Title

Mitochondrial Proteostasis Requires Genes Encoded in a Neurodevelopmental Syndrome Locus

Journal

Journal of Neuroscience, 41(31)

ISSN

0270-6474

Authors

Gokhale, Avanti
Lee, Chelsea E
Zlatic, Stephanie A
et al.

Publication Date

2021-08-04

DOI

10.1523/jneurosci.2197-20.2021

Peer reviewed

Cellular/Molecular

Mitochondrial Proteostasis Requires Genes Encoded in a Neurodevelopmental Syndrome Locus

Avanti Gokhale,[1*] Chelsea E. Lee,[1*] Stephanie A. Zlatic,[1*] Amanda A. H. Freeman,[1,2] Nicole Shearing,[1] Cortnie Hartwig,[1] Oluwaseun Ogunbona,[3] Julia L. Bassell,[1] Meghan E. Wynne,[1] Erica Werner,[1] Chongchong Xu,[4] Zhexing Wen,[1,4] Duc Duong,[5] Nicholas T. Seyfried,[5] Carrie E. Bearden,[6] Viktor János Oláh,[1] Matthew J. M. Rowan,[1] Jill R. Glausier,[7] David A. Lewis,[7] and Victor Faundez[1]

[1]Departments of Cell Biology, [2]Center for the Study of Human Health, [3]Pathology, [4]Psychiatry and Behavioral Sciences, [5]and Biochemistry, Emory University, Atlanta, Georgia 30322, [6]Semel Institute for Neuroscience and Human Behavior Department of Psychology, UCLA, Los Angeles, California 90095, and [7]Departments of Psychiatry and Neuroscience, University of Pittsburgh, Pittsburgh, Pennsylvania 15213

Eukaryotic cells maintain proteostasis through mechanisms that require cytoplasmic and mitochondrial translation. Genetic defects affecting cytoplasmic translation perturb synapse development, neurotransmission, and are causative of neurodevelopmental disorders, such as Fragile X syndrome. In contrast, there is little indication that mitochondrial proteostasis, either in the form of mitochondrial protein translation and/or degradation, is required for synapse development and function. Here we focus on two genes deleted in a recurrent copy number variation causing neurodevelopmental disorders, the 22q11.2 microdeletion syndrome. We demonstrate that SLC25A1 and MRPL40, two genes present in the microdeleted segment and whose products localize to mitochondria, interact and are necessary for mitochondrial ribosomal integrity and proteostasis. Our *Drosophila* studies show that mitochondrial ribosome function is necessary for synapse neurodevelopment, function, and behavior. We propose that mitochondrial proteostasis perturbations, either by genetic or environmental factors, are a pathogenic mechanism for neurodevelopmental disorders.

Key words: **22q11.2; mitochondria; neurodevelopmental; protein synthesis; schizophrenia; synapse; CNV**

Significance Statement

The balance between cytoplasmic protein synthesis and degradation, or cytoplasmic proteostasis, is required for normal synapse function and neurodevelopment. Cytoplasmic and mitochondrial ribosomes are necessary for two compartmentalized, yet interdependent, forms of proteostasis. Proteostasis dependent on cytoplasmic ribosomes is a well-established target of genetic defects that cause neurodevelopmental disorders, such as autism. Here we show that the mitochondrial ribosome is a neurodevelopmentally regulated organelle whose function is required for synapse development and function. We propose that defective mitochondrial proteostasis is a mechanism with the potential to contribute to neurodevelopmental disease.

Introduction

Neurodevelopmental disorders offer a two-way path to understand synapses and their alterations in disease states. One conceptual path is defined by existing knowledge of gene function in synapse development, function, and plasticity. This route provides a directed way to comprehend molecular pathogenesis because gene function is known before the discovery of neurodevelopmental disorder-associated human mutations. This is the case of genes necessary for synaptic adhesion (NRX1, NLG1) or postsynaptic scaffolding (SHANK2, SHANK3) (Sudhof, 2008; Zoghbi and Bear, 2012; Han et al., 2013). On the other hand, a second path is illustrated by neurodevelopmental monogenic defects that have propelled the understanding of new synaptic mechanisms. Such is the case of Fragile X syndrome, which is an autism spectrum disorder caused by mutations in the FMR1 gene. The FMR1 gene product is required for translational repression of diverse transcripts that localize to the synapse. This

Received Aug. 21, 2020; revised June 23, 2021; accepted June 26, 2021.

Author contributions: A.G. and V.F. designed research; A.G., C.E.L., S.A.Z., A.A.H.F., N.S., C.H., O.O., J.L.B., M.E.W., E.W., C.X., Z.W., D.D., N.T.S., C.E.B., V.J.O., M.J.M.R., J.R.G., D.A.L., and V.F. performed research; A.G., C.E.L., A.A.H.F., D.D., and V.F. analyzed data; A.G., C.E.L., S.A.Z., A.A.H.F., O.O., J.L.B., M.E.W., E.W., Z.W., N.T.S., C.E.B., M.J.M.R., J.R.G., D.A.L., and V.F. edited the paper; V.F. wrote the first draft of the paper; V.F. wrote the paper.

This work was supported by National Institutes of Health Grant 1RF1AG060285 to V.F., Emory Catalyst Grant, Accelerating Medicine Partnership AD Grant U01AG061357, and National Institute on Aging Grant RF1AG053960. M.E.W. was supported by National Institutes of Health Grants F31AG067623 and 5T32NS007480. Stocks obtained from the Bloomington *Drosophila* Stock Center (National Institutes of Health P40OD018537) were used in this study. We thank members of the V.F. laboratory for comments. V.F. thanks Maria Olga Gonzalez for providing mitochondria.

*A.G., C.E.L., and S.A.Z. contributed equally to this work.

The authors declare no competing financial interests.

Correspondence should be addressed to Victor Faundez at vfaunde@emory.edu or Avanti Gokhale at avanti.gokhale@gmail.com.

https://doi.org/10.1523/JNEUROSCI.2197-20.2021

fact opened the door to uncover novel synaptic protein translation requirements for normal synapse development, function, and plasticity, which are tied to cytoplasmic ribosomes (Sutton and Schuman, 2006; Bassell and Warren, 2008; Suhl et al., 2014). While monogenic disorders exemplify an opportunity to discover new synaptic mechanisms, these monogenic defects account for a small proportion of all genetic defects associated with neurodevelopmental disorders (Lee et al., 2020).

We focused on frequent and less explored mutations conferring risk of neurodevelopmental disorders known as chromosomal microdeletions or copy number variations (Malhotra and Sebat, 2012; Kirov, 2015; Rutkowski et al., 2017). Microdeletions are complex genetic defects that create haploinsufficiencies in multiple contiguous genes within a chromosomal segment and are among the strongest genetic risk factors for some neurodevelopmental disorders, such as schizophrenia, increasing disorder risk up to 25-fold (McDonald-McGinn et al., 2015; Rutkowski et al., 2017). This is the case of the 22q11.2 microdeletion syndrome, a genetic defect that produces a haploinsufficiency of 46 protein-coding genes and 17 small regulatory RNAs contained in the 22q11.2 chromosome band (Jonas et al., 2014; Guna et al., 2015; McDonald-McGinn et al., 2015). The frequency, penetrance, and diversity of neurodevelopmental phenotypes associated with microdeletion syndromes strongly argue that these complex genetic defects hold important, yet unknown, clues about mechanisms required for synapse development, function, and plasticity. This premise prompted us to interrogate in an unbiased manner the biological mechanisms that require the function of individual 22q11.2 microdeleted genes. We report that two genes encoded within the 22q11.2 locus and that localize to mitochondria, SLC25A1 (Solute Carrier Family 25 Member 1) and MRPL40 (Mitochondrial Ribosomal Protein L40), biochemically and genetically interact to sustain mitochondrial proteostasis.

Mitochondrial protein homeostasis, or proteostasis, is the state and mechanisms that maintain the balance of protein synthesis and degradation in mitochondria (Pickles et al., 2018). Mitochondrial protein translation contributes to mitochondrial proteostasis integrating the mitochondrial and nuclear genomes, which are necessary for the synthesis and assembly of a functional respiratory chain (Taanman, 1999; Wallace, 2010; Couvillion et al., 2016). While defective mitochondrial proteostasis has been linked to neurodegenerative diseases and the control of lifespan (Houtkooper et al., 2013; Sun et al., 2016; Pickles et al., 2018; Liu et al., 2020, 2020), there is little indication that mitochondrial proteostasis, either in the form of mitochondrial protein translation and/or degradation, is required for synapse development and function (Lottes and Cox, 2020). Here we evaluate whether SLC25A1 and MRPL40, two 22q11.2 encoded genes, are necessary for mitochondrial ribosome stability, proteostasis, and synaptic integrity. SLC25A1 is an inner mitochondrial membrane transporter required for the transport of citrate from the mitochondrial matrix to the cytoplasm (Nota et al., 2013; Palmieri, 2014; Ogunbona and Claypool, 2019; Ruprecht and Kunji, 2019). So far, there is no evidence that SLC25A1 participates in mitochondrial ribosome-dependent protein synthesis. In contrast, MRPL40 is a protein of the large subunit of the mitochondrial ribosome whose function is necessary for mitochondrial protein synthesis in eukaryotes (Jia et al., 2009; Amunts et al., 2014). MRPL40 is present in synaptic fractions where it could influence synaptic activity (Maynard et al., 2008). Indeed, MRPL40 haploinsufficiency is enough to perturb synaptic plasticity by disruption of mitochondrial calcium buffering, but whether MRPL40's mitochondrial ribosome-dependent function is required for neurodevelopment remains unexplored (Devaraju et al., 2017). We demonstrate that deletion of human SLC25A1 compromises the integrity of the mitochondrial ribosome, downregulating the expression of multiple ribosome subunits, including MRPL40. This loss of mitochondrial ribosomes compromises the expression of mitochondrial genome-encoded transcripts requiring mitochondrial ribosomes for their translation. Furthermore, we determined that mitochondrial ribosome function is necessary for synapse neurodevelopment in *Drosophila*. We propose that mitochondrial proteostasis perturbations, by genetic, environmental factors, or xenobiotics such as antibiotic exposure, contribute to the pathogenesis of neurodevelopmental disorders.

Material and Methods

Cell lines and culture conditions

Gene-edited isogenic cell lines (HAP1 cells) null for either SLC25A1 (HZGHC001753c003 and HZGHC001753c010) or SLC25A4 (HZGHC000778c011) were obtained from Horizon (RRID:CVCL_5G07; RRID:CVCL_TM04; RRID:CVCL_TM05; RRID:CVCL_TM45). The cell lines were grown and maintained in IMDM (Lonza Walkersville, 12-722F) containing 10% FBS and 100 μg/ml penicillin and streptomycin at 37°C in a 10% CO_2 incubator. Neuroblastoma SH-SY5Y cells (ATCC, CRL-2266; RRID:CVCL_0019) were grown in DMEM with 10% FBS and 100 μg/ml penicillin and streptomycin at 37°C in 10% CO_2. To produce stable cell lines, SH-SY5Y cells were transfected either with a control empty vector (GeneCopoeia, EX-NEG-Lv102) or ORF expression clone containing N terminally tagged FLAG-SLC25A1 (GeneCopoeia, EX-A1932-Lv1020GS) or C terminally tagged Myc-DDK MRPL40 (Origene, RC202166). The stably transfected cell lines were selectively maintained in media containing DMEM supplemented with 10% FBS, 100 μg/ml penicillin and streptomycin, and puromycin 2 μg/ml (Invitrogen, A1113803) or neomycin 0.2 mg/ml (Hyclone, SV30068), respectively, at 37°C in 10% CO_2. Differentiated SH-SY5Y cells were grown on poly-L-lysine (Sigma, P4707)-coated coverslips. Growth media was exchanged for differentiation media consisting of neurobasal media (Invitrogen, 21103049) supplemented with B-27 (Invitrogen, 17504-044), 500 μM L-glutamine (Thermo Fisher Scientific, SH30034.01) and 1 mM dibutyryl cyclic-AMP (Sigma, D0260), for 3 d while incubating at 37°C with 5% CO_2 (Kume et al., 2008). DU145 (ATCC, catalog #HTB-81, RRID:CVCL_0105) and Rho0 cells were prepared and donated by Erica Werner and John Petros (Marullo et al., 2013). These cell lines grow in RPMI (catalog #11875-093) 10% FBS and 100 μg/ml penicillin and streptomycin. Additionally, the media for Rho0 cells needed to be supplemented by sterile 0.2 mM uridine, 1 mM sodium pyruvate, and 11 mM glucose.

SH-SY5Y CRISPR-Cas9 mutagenesis

Genome editing was performed by transfection of Cas9-gRNA ribonucleoprotein complexes by Synthego. Mutagenesis was performed with the guide RNA sequence GGGTTCCCGGTCC CTGCAGG targeting transcript ID: ENST00000215882 Exon 2. An Editing efficiency was of 95%. Edited cells were cloned by limited cell dilution and single clones confirmed by Sanger sequencing.

SH-SY5Y and primary neuron immunofluorescence

Differentiated SH-SY5Y cells were PFA fixed for immunofluorescent probing. All steps were completed at 37°C with prewarmed reagents. Cells were washed twice in PBS containing 0.1

mM $CaCl_2$ and 1.0 mM $MgCl_2$, then fixed for 20 min in 4% PFA in PBS. Cells were permeabilized for 5 min in 0.2% Triton X-100 in PBS and blocked for 30 min in 20% FBS in PBS. Primary and secondary antibodies were diluted in blocking solution and incubated for 30 min each (anti-SLC25A1 1:200 PTG #15235-1, anti-FLAG 1:200 Sigma, #F3165, anti-mouse AlexaFluor-555 1:1000 Invitrogen #A21455, anti-rabbit AlexaFluor-488 1:1000 Invitrogen A11034). Coverslips were mounted with DAPI Fluoromount (Southern Biotechnology, 0100-20). *Z*-stack images were captured with NIS Elements on a Nikon A1R HD25 confocal microscope with a 60× oil immersion objective (NA 1.4, Apo, DIC) and 402, 488, and 561 nm laser lines.

Glass coverslips of E18 Sprague Dawley rat hippocampal cultures were obtained from BrainBits (catalog #ANHP12mm-2) and cultured at 37°C, 5% CO_2, in NbActiv4 media. MRPL40-HA plasmid (Genecopoia EX-T0232-M07) was transfected in hippocampal cultures with FuGENE HD transfection reagent (Promega E2311) in a 3:1 ratio (reagent:DNA) following the manufacturer's protocol. Cultures were incubated overnight with a 30 μl volume of reagent:DNA mixture/500 μl media in wells of 24 well dishes. Fresh media was exchanged 24 h after transfection, and cultures were fixed for immunofluorescence 48 h after transfection. For coverslips treated with MitoTracker Green FM (catalog #M7514 Invitrogen), a 1:1000 dilution was incubated in culture media at 37°C, 5% CO_2, for 30 min followed by fixation for immunofluorescence. All coverslips were fixed at 37°C in 4% PFA for 20 min, permeabilized with 0.2% Triton X-100 in PBS for 5 min, and blocked with 2% BSA, 1% fish gelatin, and 15% horse serum in PBS for 30 min. Primary and secondary antibodies were each diluted in blocking solution and incubated on coverslips for 30 min at 37°C. Coverslips were mounted with DAPI-Fluoromount-G (Southern Biotechnology, catalog #0100-20). Antibody dilutions were as follows: rabbit anti-SLC25A1 1:200 (PTG, 15235-1-AP) rat anti-HA 1:500 (Roche, 11867423001), goat anti-rabbit AlexaFluor-555 1:1000 (Invitrogen, A21429), and goat anti-rat Oregon Green 1:1000 (Invitrogen, O6382). Fixed neurons were imaged on a Nikon A1R HD25 Inverted Ti2-E; confocal microscope with an Apo 60× oil λS DIC N2 objective, NA 1.4, Galvano laser scanner, and multi-alkali and GaAsp PMT detectors. Laser excitation wavelength of fluorophores occurred at 405.0, 488.0, and 561.0 nm and emission detection with 450/50, 525/50, and 595/50 cubes. *Z* stacks with a 0.15 μm step were projected for max intensity in Fiji.

Seahorse metabolic oximetry

Protocol is based on Divakaruni et al. (2014). HAP1 (40,000 cells/well) and DU145/Rho0 (30,000 cells/well) were plated on Agilent Technologies, Seahorse XF96 V3-PS Microplates (Agilent Technologies, 101085-004) ~24 h before stress tests. In the case of 48 h drug treatment, cells were treated in culture for 24 h and then plated to 96 well microplates for the final 24 h of treatment. Drugs used were doxycycline (Sigma, D9891), minocycline (Sigma, M9511), chloramphenicol (Sigma, C0378), linezolid (Sigma, PZ0014), actinonin (Sigma, A6671), and carbenicillin (Sigma, C1389). Drug concentrations were as described in the figures and text. Seahorse XFe96 FluxPaks (Agilent Technologies, 102416-100) were hydrated at 37°C for ~24 h in Seahorse XF Calibrant solution (Agilent Technologies, 100840-000). The cellular mitochondrial stress test was run as per Agilent Technologies, Seahorse protocols with Seahorse Wave Software (Agilent Technologies). Stress test media consisted of Seahorse XF Base Medium (Agilent Technologies, 102353-100) supplemented with 10 mM D-glucose (Sigma, G8769), 1 mM sodium pyruvate (Sigma, S8636), and 2 mM L-glutamine (HyClone SH30034.01) and brought to pH 7.4 with sodium hydroxide (Thermo Fisher Scientific, S318). Cells were incubated with stress test media for 1 h before stress test assay at 37°C without CO_2 injection. Seahorse Wave Software data collection was as per default conditions. Flux Plate probes were loaded and calibrated. The utility plate containing calibrant was then exchanged for the Seahorse cell culture plate and equilibrated as per protocol. Oxygen consumption rates and extracellular acidification rates were collected 3 times for each phase of the stress test with a 3 min mix step followed by 3 min of measurement. FluxPak ports were loaded at a 10× concentration of the final well concentration, as per the stress test protocol. Well concentrations of stress test drugs were 1-2 μM oligomycin A (Sigma, 75351), 0.125 μM FCCP (Hap1 cells), and 0.25 μM (DU145/Rho0 Cells) (Sigma, C2920), 0.5 μM rotenone (Sigma, R8875), and 0.5 μM antimycin A (Sigma, A8674). All Seahorse microplates were normalized by total protein using the Pierce BCA Protein Assay Kit (Thermo Fisher Scientific, 23227) as per protocol with a BSA protein standard. The BCA assay absorbance was read by a BioTek microplate reader using Gen5 software. Seahorse oximetry data analysis was done with Agilent Technologies, Wave Software Report Generator, and Microsoft Excel. At least three replicates were done for every condition tested.

Crystal violet assay

DU145 (5000 cells/well) and DU145 Rho0 (20,000 cells/well) were grown on 96 well culture plates with doxycycline (Sigma, 9891) concentrations ranging from 0 to 25 μM. After 48 h, cells were washed once with PBS (Corning, 21-040-CV) supplemented with 0.1 mM $CaCl_2$ and 1.0 mM $MgCl_2$. Cells were then fixed at room temperature for 5 min with 65% methanol followed by fixation for 15 min with 100% methanol. Methanol was removed and plates were dried overnight followed by 5 min stain with 0.1% crystal violet in Milli-Q water. Stain was removed, washed 3 times with water, and air dried. Captured crystal violet was solubilized in 2% deoxycholate in water and incubated on an orbital shaker at room temperature for 10 min. Absorbance was read on a BioTek microplate reader with Gen5 software (Feoktistova et al., 2016; Comstra et al., 2017).

Cell lysates, immunoprecipitation, and membrane extraction

HAP1 or SH-SY5Y cells were grown in 10 cm tissue culture dishes, placed on ice, and rinsed twice with cold PBS (Corning, 21-040-CV) supplemented with 0.1 mM $CaCl_2$ and 1.0 mM $MgCl_2$. Cells were scraped from the tissue culture dishes, placed in Eppendorf tubes in lysis buffer containing 150 mM NaCl, 10 mM HEPES, 1 mM EGTA, and 0.1 mM $MgCl_2$, pH 7.4 (Buffer A) with 0.5% Triton X-100 and Complete anti-protease (Roche, 11245200). Cell homogenates were incubated on ice for 30 min and centrifuged at 16,100 × *g* for 10 min, and the clarified supernatant was recovered. Bradford Assay (Bio-Rad, 5000006) was used to determine protein concentration. If the cell lysates were used for immunoprecipitation, 500 µg of the soluble protein extract was incubated with 30 µl Dynal magnetic beads (Invitrogen, 110.31) coated with 1 µg of required antibodies and washed from excess antibody. The mixture was incubated on an end-to-end rotator for 2 h at 4°C. In some cases, as controls, the immunoprecipitation was outcompeted with the 3XFLAG peptide (340 μM; Sigma, F4799). Beads were then washed 6 times

with Buffer A with 0.1% Triton X-100 followed by elution with Laemmli buffer. Samples were then analyzed by SDS-PAGE, immunoblot, or silver stain (Gokhale et al., 2012, 2019). Immunoprecipitation from fractionated brain extracts was performed as described above with the following modifications: 500 µg of P1 fractions was applied to 30 µl of Dynal beads coated with the MRPL40 antibody. For outcompetition, MRPL40 peptide conjugated to a His Tag was used (2 µg; Proteintech Group, Ag10477). The beads were washed and eluted with Laemmli sample buffer as described above.

To prepare membrane-enriched fractions, cells were lifted from dishes using ice-cold PBS containing 10 mM EDTA. Cells were pelleted at 800 × *g* for 5 min and resuspended in 5 mM HEPES containing Complete antiprotease. The lysate was then sonicated and incubated on ice for 30 min followed by ultracentrifugation in a TLA120.2 rotor at 68,000 RPM at 4°C for 30 min. The supernatant was discarded, and the cell pellets were dissolved in 0.1 M sodium carbonate at pH 11 containing Complete Antiprotease (Fujiki et al., 1982). The lysate was sonicated and placed on ice for 30 min followed by ultracentrifugation at 68,000 RPM for 30 min at 4°C. The supernatant was discarded; the pellet was washed twice with ice-cold PBS to remove remnants of the sodium carbonate solution. The pellet was dissolved in the lysis buffer described above, sonicated, placed on ice for 30 min followed by centrifugation at 16,100 × *g* for 10 min, and the clarified supernatant was recovered. Protein concentrations were determined using the Bradford assay, and equivalent amounts were loaded on SDS-PAGE gels for further analysis.

Immunoblotting

Equivalent amounts or volumes of cell lysates were reduced and denatured with Laemmli buffer (SDS and 2-mercaptoethanol) and heated for 5 min at 75°C. Samples were then loaded onto 4%-20% Criterion gels (Bio-Rad, 5671094) for SDS-PAGE and transferred to PVDF membrane (Millipore, IPFL00010) using the semidry transfer method. The membranes were then incubated with TBS containing 5% nonfat milk and 0.05% Triton X-100 (TBST; blocking solution) for 30 min at room temperature, rinsed, and incubated overnight with optimally diluted primary antibody in a buffer containing PBS with 3% BSA and 0.2% sodium azide. Membranes were then rinsed in TBST. HRP-conjugated secondary antibody diluted 1:5000 in the blocking solution was then added to the membranes for at least 30 min at room temperature. The membranes were then rinsed in TBST 3 times and then treated with Western Lightning Plus ECL reagent (PerkinElmer, NEL105001EA) and exposed to GE Healthcare Hyperfilm ECL (28906839) (Gokhale et al., 2012, 2019).

Total RNA extraction, cDNA preparation, and qRT-PCR

Total RNA was extracted from cells or *Drosophila* using Trizol reagent (Invitrogen, 15596026). Cells or animals were washed twice in PBS with 0.1 mM $CaCl_2$ and 1.0 mM $MgCl_2$, and 1 ml of Trizol was added to the samples and incubated for 10 min at room temperature on an end-to-end rotator; 200 µl of chloroform was added to each tube; and after a brief incubation, the mixture was centrifuged at 12,000 RPM for 15 min at 4°C. The aqueous layer was collected, 500 µl of isopropanol was added to it, and the mixture was rotated for 10 min at room temperature followed by centrifugation at 12,000 rpm for 15 min. The supernatant was discarded, and the pellet washed with 75% ethanol. After air drying, the pellet was dissolved in 20 µl of molecular grade RNAase-free water. RNA was quantified and the purity determined using the Bio-Rad SmartSpec Plus Spectrophotometer or the Nanodrop One^C (Thermo Fisher Scientific). cDNA was synthesized using 5 µg RNA as a template per reaction using the Superscript III First Strand Synthesis System Kit (Invitrogen, 18080-051) and random hexamer primers using the following protocol. RNA was incubated with the hexamers, dNTPs at 65°C for 5 min; the samples were placed on ice; and a cDNA synthesis mix was added to each of the tubes. These samples were then subjected to the following protocol: 25°C for 10 min followed by 50 min at 50°C. The reaction was terminated 85°C for 5 min and the samples treated with RNase H at 37°C for 20 min.

For RT-PCR, IDT Real-Time qPCR Assay Entry site was used to design the primers. Primers were synthesized by Sigma-Aldrich Custom DNA Oligo service. Primer annealing and melting curves were used to confirm optimal primer quality and specificity to single transcripts. The primer list is provided in Extended Data Fig. 2-1; 1 µl of the newly synthesized cDNA was then used to perform qRT-PCR in LightCycler 480 SYBR Green I Master (Roche, 04707516001) according to the protocol below on a LightCycler 480 Instrument or the QuantStudio 6 Flex instrument (Applied Biosystems) in a 96 well format. The qRT-PCR experimental protocol includes initial denaturation at 95°C for 5 min, followed by 45 cycles of amplification with a 5 s hold at 95°C ramped at 4.4°C/s to 55°C. Temperature is maintained for 10 s at 55°C and ramped up to 72°C at 2.2°C/s. Temperature was held at 72°C for 20 s where a single acquisition point was collected and then ramped at 4.4°C/s to begin the cycle anew. The temperature was then held at 65° for 1 min and ramped to 97°C at a rate of 0.11°C/s. Five acquisition points were collected per °C. Standard curves collected for individual primer sets were used for quantification using LightCycler 480 or the QuantStudio RT-PCR Software version 1.2. Data were normalized using reference genes and presented as a ratio of control to experimental samples.

Mitochondrial genome measurements

We followed the procedures by Rooney et al. (2015). Cells were grown on 10 cm dishes, and total genomic DNA was isolated using the DNeasy Blood and Tissue kit following the manufacturer's instructions (QIAGEN, catalog #69504). DNA was quantified using the Nanodrop One^C and diluted to 3 ng/µl for all cell lines; 2 µl of template DNA, 400 nM of mitochondrial or nuclear genome specific primers (listed in Extended Data Fig. 2-1, Mt-tRNA-Leu (UUR)) and Nuclear-Beta2-microglobulin respectively), 12.5 µl of SYBR Green I Master, and 8.5 µl of nuclease-free water were added per well of a 96 well dish. Each sample was then amplified using the following protocol: 50°C for 2 min followed by 95°C for 10 min. The samples were amplified over 40 cycles of 95°C for 15 s and using primer specific annealing temperature of 62°C for 60 s. Melting curve analysis was used to ensure specificity of a single PCR product. The experiment was done at a minimum in triplicate using Applied Biosystems QuantStudio 6 Flex Real-Time PCR System Instrument and the QuantStudio RT-PCR software version 1.2 software provided a cycle threshold value (C_t) for each cell line and primer set. Mitochondrial DNA was quantified relative to nuclear DNA content using the following formula: first, the difference in relative C_t was measured (δC_t) = (Nuclear DNA C_t) – (Mitochondrial DNA C_t). Relative mitochondrial DNA = $2 \times 2^{\Delta CT}$.

Mitochondrial ribosome sucrose gradient fractionation

Cells grown in 10 cm dishes were washed twice with ice-cold PBS and pelleted at 800 RPM for 5 min. The cell pellet was lysed in a Mitolysis buffer containing 10 mM Tris, pH 7.5, 100 mM

KCl, 2% Triton X-100, 5 mM β-mercaptoethanol, 20 mM $MgCl_2$, and Complete EDTA-free antiprotease (Roche, 11245200). After sonication, cells were placed on ice for 30 min and centrifuged at 12,000 rpm for 15 min at 4°C. The soluble supernatant was recovered, and protein content was measured using the Bradford assay; 500 µg of protein was loaded on a continuous 10%-30% sucrose gradient buffered in 10 mM Tris, pH 7.5, 100 mM KCl, 0.02% Triton X-100, 5 mM β-mercaptoethanol, and 20 mM $MgCl_2$ and Complete EDTA-free Antiprotease (Matthews et al., 1982). Sucrose gradients were centrifuged at 70,000 × *g* for 16 h in an SW55 rotor. Individual fractions were collected from the bottom of the gradient, and equal volumes were denatured and reduced with Laemmli buffer. Equal volumes of alternate fractions were resolved by SDS-PAGE for either protein stains or immunoblots.

Identical procedures were performed for brain Percoll-enriched mitochondrial fractions. Each gradient was loaded with 500 µg of soluble mitochondrial protein extracted with Mitolysis buffer.

Ribosome sucrose gradient fractionation

Cells were grown in 10 cm dishes at 37°C and 10% CO_2. The following protocol was followed (Aboulhouda et al., 2017): On the day of the experiment, 100 µg/ml cycloheximide was added to each plate, and the cells were incubated at 37°C for 10 min. Plates were then placed on ice and washed twice with ice-cold PBS. Cells were then scraped and transferred into an Eppendorf tube and pelleted at 500 × *g* for 5 min at 4C. Cells were then lysed in a buffer containing 20 mM HEPES-KOH, pH 7.4, 5 mM $MgCl_2$, 100 mM KCl, and 200 μg/ml heparin, 1% Triton X-100, 2 mM DTT, 100 µg/ml cycloheximide, 20 U/ml Superase-IN, and Complete EDTA-free Protease Inhibitor and placed on ice for 10 min. The lysate was then centrifuged for 10 min at 4C at 12,000 × *g*. The clarified supernatant was then measured for protein content using the Bradford assay; 500 μg of total protein was then loaded onto a 10%-50% sucrose gradient buffered with 20 mM HEPES-KOH, pH 7.4, 5 mM $MgCl_2$, 100 mM KCl, 2 mM DTT, 100 μg/ml cycloheximide, and 20 U/ml Superase-IN. The samples were then ultracentrifuged in SW55 Ti rotor at 160,000 × *g* for 2.5 h at 4°C. Fractions were collected from the bottom, denatured, and reduced in Laemmli buffer. Equal volumes of alternate fractions were then analyzed on SDS PAGE by protein stain and immunoblot.

Synaptosome preparation

Synaptosomes were prepared by Percoll sedimentation as described previously (Nagy and Delgado-Escueta, 1984; Faundez et al., 1992). We quantified protein content in selected fractions using label-free quantitative mass spectrometry as described below. We determined the proteome of P1 fractions, heavy synaptosomes, mitochondria, and the sucrose gradient-enriched mitochondrial fraction described in Extended Data Fig. 2-2*B*. Protein abundance, measured as ion intensities, was normalized to the sum of all protein ion intensities in the fraction (normalized protein abundance). We used the P1 pellet normalized protein abundances as a denominator to calculate relative enrichment of a protein of interest in heavy synaptosomes, mitochondria, and the sucrose gradient-enriched mitochondrial fraction. Increases in the relative content of a protein describe a reduction in the complexity of a fraction as well as the enrichment of a particular protein. The mass spectrometry proteomics data have been deposited to the ProteomeXchange Consortium via the PRIDE (Perez-Riverol et al., 2016) partner repository with the dataset identifier PXD025289.

Mass spectrometry of immunoprecipitates and sucrose gradient fractions

Services were provided by MS Bioworks. Immunoprecipitates were separated ~1.5 cm on a 10% Bis-Tris Novex mini-gel (Invitrogen) using the MES buffer system. The gel was stained with Coomassie and excised into 10 equally sized segments. Gel segments were processed using a robot (ProGest, DigiLab) with the following protocol: washed with 25 mM ammonium bicarbonate followed by acetonitrile, reduced with 10 mM TTT at 60° C followed by alkylation with 50 mM iodoacetamide at room temperature, digested with trypsin (Promega) at 37°C for 4 h, and quenched with formic acid; and the supernatant was analyzed directly without further processing. The gel digests were analyzed by nano LC-MS/MS with a Waters NanoAcquity HPLC system interfaced to a Thermo Fisher Scientific Q Exactive. Peptides were loaded on a trapping column and eluted over a 75 μm analytical column at 350 nl/min; both columns were packed with Luna C18 resin (Phenomenex). The mass spectrometer was operated in data-dependent mode, with MS and MS/MS performed in the Orbitrap at 70,000 FWHM resolution and 17,500 FWHM resolution, respectively. The 15 most abundant ions were selected for MS/MS.

Sucrose fraction protein quantitation was performed using Qubit fluorimetry (Invitrogen). An equal volume (55 μl; 21.7 μg C-1 and 7.9 μg 10-1) of each sample was separated on a 10% Bis-Tris Novex mini-gel (Invitrogen) using the MES buffer system. The gel was stained with Coomassie, and each lane was excised into 20 equally sized segments. Gel pieces were processed using a robot (ProGest, DigiLab). Each gel digest was analyzed by nano LC-MS/MS with a Waters M-class HPLC system interfaced to a Thermo Fisher Scientific Fusion Lumos. Peptides were loaded on a trapping column and eluted over a 75 μm analytical column at 350 nl/min; both columns were packed with XSelect CSH C18 resin (Waters); the trapping column contained a 3.5 μm particle, and the analytical column contained a 2.4 μm particle. The column was heated to 55°C using a column heater (Sonation). A 30 min gradient was used (10 h LC-MS/MS total per sample). The mass spectrometer was operated in data-dependent mode, with MS and MS/MS performed in the Orbitrap at 60,000 FWHM resolution and 15,000 FWHM resolution, respectively. APD was turned on. The instrument was run with a 3 s cycle for MS and MS/MS.

For immunoprecipitates and sucrose fractions, data were searched using a local copy of Mascot with the following parameters: Enzyme: Trypsin. Database: Swissprot Human (concatenated forward and reverse plus common contaminants). Fixed modification: Carbamidomethyl (C). Variable modifications: Oxidation (M), Acetyl (Protein N-term), Deamidation (NQ), Pyro-Glu (N-term Q). Mass values: Monoisotopic. Peptide Mass Tolerance: 10 ppm. Fragment Mass Tolerance: 0.02 Da. Max Missed Cleavages: 2. Mascot DAT files were parsed into the Scaffold software for validation, filtering, and to create a non-redundant list per sample. Data were filtered at 1% protein and peptide level FDR and requiring at least two unique peptides per protein.

Tandem mass tagging (TMT)

Samples for TMT analysis were prepared as follows. Cells were grown in 10 cm dishes to 85%-90% confluency. On the day of the experiment, the cells were placed on ice and washed 3 times

with PBS supplemented with 10 mM EDTA (Sigma, 150-38-9) for 3 min each. After the third wash, the cells were incubated with PBS and 10 mM EDTA for 30 min on ice. Cells were then lifted with mechanical agitation using a 10 ml pipette and collected in a 15 ml Falcon tube. Cells were then spun at 800 × *g* for 5 min at 4°C. The supernatant was then aspirated out, and the remaining pellet was washed with ice-cold PBS. The resuspended cells were then centrifuged at 16,100 × *g* for 5 min. The supernatant was discarded, and the resulting pellet was immediately frozen on dry ice for at least 5 min and stored at −8°C for future use.

A total of 16 individual and 2 pooled standards were analyzed across two TMT 10-plex batches. Samples ($n = 16$) were randomized into two batches and labeled using 10-plex TMT reagents. Two pooled standards were included in each batch to assess the reproducibility of (Ping et al., 2018). For sample to batch arrangement, see Data availability. TMT labeling was performed as described. In brief, TMT reagent (5 mg) was dissolved in 56 μl anhydrous ACN. Each peptide solution was then reconstituted in 400 μl 100 mM TEAB buffer and 164 μl (3.2 mg) of labeling reagent subsequently added. After 1 h, the reaction was quenched with 32 μl of 5% hydroxylamine. After labeling, the peptide solutions were combined according to the batch arrangement. Each TMT batch was then desalted with 500 mg C18 Sep-Pak columns (Waters), and eluted peptides were dried by speed vacuum (Labconco).

High pH fractionation

All TMT batches were subjected according to high pH fractionation (Higginbotham et al., 2019). For each batch, ~4 mg of TMT-labeled peptides was resuspended in 850 μl loading buffer (1 mM ammonium formate, 2% (v/v) ACN), injected completely with an autosampler, and fractionated using a ZORBAX 300Extend-C18 column (4.6 mm × 250 mm, 5 μm, Agilent Technologies) on an Agilent Technologies, 1100 HPLC system monitored at 280 nm. A total of 96 fractions were collected over a 96 min gradient of 100% mobile Phase A (4.5 mM ammonium formate, pH 10, in 2% v/v acetonitrile) from 0 to 7 min, 0%-16% mobile Phase B (4.5 mM ammonium formate, pH 10, in 90% v/v acetonitrile) from 7 to 13 min, 16%-40% B from 13 to 73 min, 40%-44% from 73 to 77 min, 44%-60% B from 77 to 82 min, and 60% B until completion with a flow rate of 0.8 ml/min. The 96 fractions were collected with an even time distribution and pooled into 24 fractions.

LC-MS/MS

An equal volume of each of the 24 high-pH peptide fractions was resuspended in loading buffer (0.1% FA, 0.03% TFA, 1% ACN), and peptide eluents were separated on a self-packed C18 (1.9 μm, Maisch) fused silica column (25 cm × 75 μm internal diameter, New Objective) by an Easy-nanoLC system (Thermo Fisher Scientific) and monitored on an Orbitrap Fusion Lumos mass spectrometer (Thermo Fisher Scientific). Elution was performed over a 140 min gradient at a rate of 350 nl/min with Buffer B ranging from 1% to 90% (Buffer A: 0.1% FA in water, Buffer B: 80% ACN in water and 0.1% FA). The mass spectrometer was set to acquire data in top speed mode with 3 s cycles. Full MS scans were collected at a resolution of 120,000 (375-1500 m/z range, 4×10^5 AGC, 50 ms maximum ion time). All HCD MS/MS spectra were acquired at a resolution of 50,000 (1.2 m/z isolation width, 36% collision energy, 5×10^4 AGC target, 86 ms maximum ion time). Dynamic exclusion was set to exclude previously sequenced peaks for 15 s within a 10 ppm isolation window. Only charge states from 2+ to 7+ were chosen for tandem MS/MS.

Database search and protein quantification

Raw data files were processed using Proteome Discover Suite (version 2.1). MS/MS spectra were searched against the UniProtKB human proteome database (downloaded April 2015 with 90,411 total sequences). The Sequest HT search engine was used with the following parameters: fully tryptic specificity; maximum of two missed cleavages; minimum peptide length of 6; fixed modifications for TMT tags on lysine residues and peptide N-termini (229.162932 Da) and carbamidomethylation of cysteine residues (57.02146 Da); variable modifications for oxidation of methionine residues (15.99492 Da) and deamidation of asparagine and glutamine (0.984 Da); precursor mass tolerance of 20 ppm; and a fragment mass tolerance of 0.05 Da. The Percolator node was used to filter PSMs to an FDR of <1% using a target-decoy strategy. Following spectral assignment, peptides were assembled into proteins and were further filtered based on the combined probabilities of their constituent peptides to a final FDR of 1%. In cases of redundancy, shared peptides were assigned to the protein sequence in adherence with the principles of parsimony. Reporter ions were quantified from MS2 scans using an integration tolerance of 20 ppm with the most confident centroid setting.

Postmortem human brain expression studies

All data from the studies performed in postmortem human brain tissue have been previously published, and all methods and materials descriptions and data are publicly available. All tissue sample collection and RNA sequencing (RNASeq) details are publicly available at the Synapse database (https://www.synapse.org/#!Synapse:syn2759792/wiki/). All tissue sample collection and microarray analysis details are described in detail (Arion et al., 2015; Enwright et al., 2018), and the data are publicly available.

Drosophila Methods

Drosophila *husbandry*. *Drosophila* stocks were reared in polystyrene vials on standard fly food (900 ml milli-Q water, 48 × *g* active dry yeast, 120 × *g* cornmeal, 9 × *g* agar, 120 × *g* molasses, 2.4 × *g* tegosept, and 9 ml propionic acid). Animals were housed in a humidified, 25C incubator (Jeio Tech, IB-15G) with a 12 h light:dark cycle.

Drosophila *stocks*. Stocks were obtained from the Bloomington *Drosophila* Stock Center: C155-GAL4 (P{w[_mW. h]_GawB}elav [C155]; RRID:BDSC_458) and vglut-GAL4 (w[1118]; P{y[+t7.7] w[+mC]=GMR51B08-GAL4}attP2/TM3, Sb[1]; RRID:BDSC_48183). RNAi lines were obtained from the Vienna *Drosophila* Resource Center: UAS-seaRNAi (w[1118];+;P{GD17700}v50713/TM3,Sb; GD17700), UAS-mRpL15 RNAi (line 1, chromosome 1) (w[1118]P{GD11582}v22035;+;+; GD11582), UAS-mRpL15 RNAi (line 2, chromosome 3) (w[1118];+; P{GD11582}v45542/TM3,Sb; GD11582), and UAS-mRpL40 RNAi (w[1118];P{GD16738}v48166/CyO;+; GD16738). Ddc-GAL4 (+;+; Ddc-GAL4) was a kind gift from A. Vrailas-Mortimer (Illinois State University). Canton S was a kind gift from M. Ramaswami (Trinity College Dublin). Individual UAS and Gal4 lines were crossed to Canton S as controls to verify that the presence of the isolated transgenes and the genetic background of these individual lines was not responsible

for the phenotype observed. Additional details are in Extended Data Fig. 2-1.

Drosophila *neuromuscular microscopy.* Wandering third instar *Drosophila* larvae were filleted using a dorsal incision to expose the neuromuscular junction on muscle VI-VII. Dissections were completed in calcium-free HL3 Ringer's solution (in mM as follows: 70 NaCl, 5 KCl, 21.5 $MgCl_2$, 10 $NaHCO_3$, 5 trehalose, 115 sucrose, 5 BES, pH 7.2-7.3) and pelts were fixed in 4% PFA at room temperature for 45 min to 1 h. After a 10 min rinse with PBS, including 0.15% Triton (PBS-T), pelts were incubated overnight at 4°C with FITC-HRP conjugate antibody (1:500, MP Bio catalog #0855977, RRID:AB_2334736). Pelts were then rinsed 9 times with PBS-T (3 1 min washes, 3 10 min washes, and 3 1 min washes) on a mini-100 orbital genie (Scientific Industries) at room temperature, mounted on slides using Vectashield mounting media (Vector Labs), coverslips were secured with nail polish, and samples were stored in a covered container at 4C until imaging (Gokhale et al., 2019).

Drosophila *confocal imaging.* Synaptic structure of the neuromuscular junction on muscles VI-VII of the third or fourth abdominal segment (A3 or A4, respectively) was analyzed with confocal imaging. *Z*-stack images were acquired with a 20× objective on an Olympus FV1000 Confocal Microscope using a continuous wave 458,488 nm argon laser at 200 mW. Fiji software (RRID:SCR_002285) was used to Oib files to 8-bit jpegs. Images were blinded for bouton number and branch length quantification (Gokhale et al., 2019).

Drosophila *electrophysiology.* Wandering third instar, female larvae were filleted in calcium-free HL3 Ringer's solution (see *Drosophila* neuromuscular microscopy). The preparations were then rinsed in low-calcium Ringer's solution (in mM as follows: 70 NaCl, 5 KCl, 1 $CaCl_2$, 20 $MgCl_2$, 10$NHCO_3$, 5 trehalose, 115 sucrose, 5 BES in ddH2O, pH 7.2-7.3), which was used for the remainder of the electrophysiology experiments. Borosilicate glass capillary tubes (1 mm diameter, 0.58 mm internal diameter; A-M Systems, catalog #601000) were pulled to a fine tip (PN-3, Narishige) to create recording electrodes (25-50 M resistance, backfilled with 3 M KCl) and firepolished (Microforge MF-830, Narishige) suction electrodes. After severing close to the ventral ganglion, motor axons were taken up into the suction electrode, and stimulated using a model 2100 Isoplated Pulse Stimulator (A-M Systems). All recordings were obtained from muscle 6 in the second or third abdominal sections (A2 or A3, respectively) using an AxoClamp 900A amplifier, Digidata 1440A, and pClamp 10 software (Molecular Devices; RRID:SCR_011323). Evoked excitatory junction potential (EJP) amplitudes were analyzed with Clampfit 10.7 (RRID:SCR_011323) and miniature EJP (mEJP) frequency and amplitude was analyzed with Mini Analysis Program (Synaptosoft; RRID:SCR_002184) (Gokhale et al., 2019).

Drosophila *activity monitor.* Female flies were collected under CO_2 anesthesia within 72 h of eclosure and housed in polystyrene vials on standard fly food for 24 h to allow recovery from CO_2. Flies were then briefly placed on ice to slow activity before mouth pipetting individual flies into 5 mm × 65 mm polycarbonate tubes (TriKinetics). Nutrients were provided via a 5% (w/v) sucrose and 2% agarose medium at one end of the tube. The other end of the tube was sealed with Parafilm perforated with an 18-guage needle to allow air flow. The flies were allowed to acclimate to these tubes and activity recording commenced with lights on (6:00 A.M.) the following day. Locomotor activity was recorded using DAM2 *Drosophila* Activity Monitors (TriKinetics) for 6 d at room temperature in a light-controlled cabinet with a 12 h light:dark cycle. Beam breaks were collected in 20 s intervals using the DAM System308 software (TriKinetics, RRID:SCR_016191), and sleep/wake architecture was analyzed based on 1 min bins using a custom-made Excel worksheet (Gokhale et al., 2019). Sleep-like behavior was defined as periods of inactivity 5 min or longer (Hendricks et al., 2000; Shaw et al., 2000). The *n* indicated in the graphs is the total number of animals analyzed across at least three replications.

Bioinformatic analyses

CORUM database searches and gene ontology analyses were performed with ENRICHR and Cluego (Bindea et al., 2009; Kuleshov et al., 2016). *In silico* interactome data were downloaded from Genemania predicted and physical interactions (Warde-Farley et al., 2010) and processed in Cytoscape version 3.5.1 (Shannon et al., 2003). Interactome connectivity graph parameters were generated in Cytoscape.

Statistical analyses

Experimental conditions were compared using Synergy KaleidaGraph version 4.1.3 or Aabel NG2 version 5 x64 by Gigawiz as specified in each figure.

Results

The SLC25A1 mitochondrial interactome

Microdeletion of the 22q11.2 chromosomal segment compromises the mitochondrial proteome, by unknown mechanisms, and as previously demonstrated, mitochondrial redox balance in neurons (Fernandez et al., 2019; Gokhale et al., 2019). Among the mitochondrial proteins affected by the 22q11.2 microdeletion, we selected the inner mitochondrial membrane protein SLC25A1 for further study. SLC25A1 is encoded in the 22q11.2 microdeleted segment. Notably, SLC25A1 gene defects cause intellectual disability and neuroanatomical defects in humans (OMIM:190315), and it is a high connectivity node in an *in silico* protein interaction network from 22q11.2 mutant cells (Nota et al., 2013; Palmieri, 2014; Gokhale et al., 2019; Ogunbona and Claypool, 2019; Ruprecht and Kunji, 2019).

We applied two strategies to comprehensively identify molecules that associate with SLC25A1. First, we used a SLC25A1-specific antibody raised against full-length SLC25A1 (RefSeq ID: NP_005975.1), whose specificity was established probing two different SLC25A1 null cell types by immunoblot and immunofluorescence (Fig. 1*A*; Extended Data Fig. 1-1*A-C*). We immunoisolated endogenous SLC25A1 with this SLC25A1 antibody either from WT or genome edited SLC25A1 null cells. We complemented these experiments with immunoaffinity isolation of FLAG-tagged SLC25A1 stably expressed at low levels in SH-SY5Y neuroblastoma cells (Fig. 1*B*, compare Lanes 1 and 2). We minimized spurious interactions with FLAG beads first by eluting protein complexes with FLAG peptide (Fig. 1*B*, Lane 2). Second, we performed control experiments where FLAG peptide outcompeted FLAG-SLC25A1 protein complexes binding to beads before FLAG peptide elution (Fig. 1*B*, Lane 3). We previously validated these strategies for other membrane-inserted proteins (Perez-Cornejo et al., 2012; Ryder et al., 2013; Comstra et al., 2017). A total of four independent experiments identified 123 proteins enriched with the SLC25A1-specific antibody from WT cells compared with SLC25A1 null cells (Fig. 1*C*,*E*; Extended Data Fig. 1-2). Twelve of these proteins were consistently identified in all four experiments, including the mitochondrial proteins ACLY, CPT1A, LDHB, RARS, and SLC25A1 (Fig. 1*E*). One FLAG pulldown experiment identified 575 proteins that

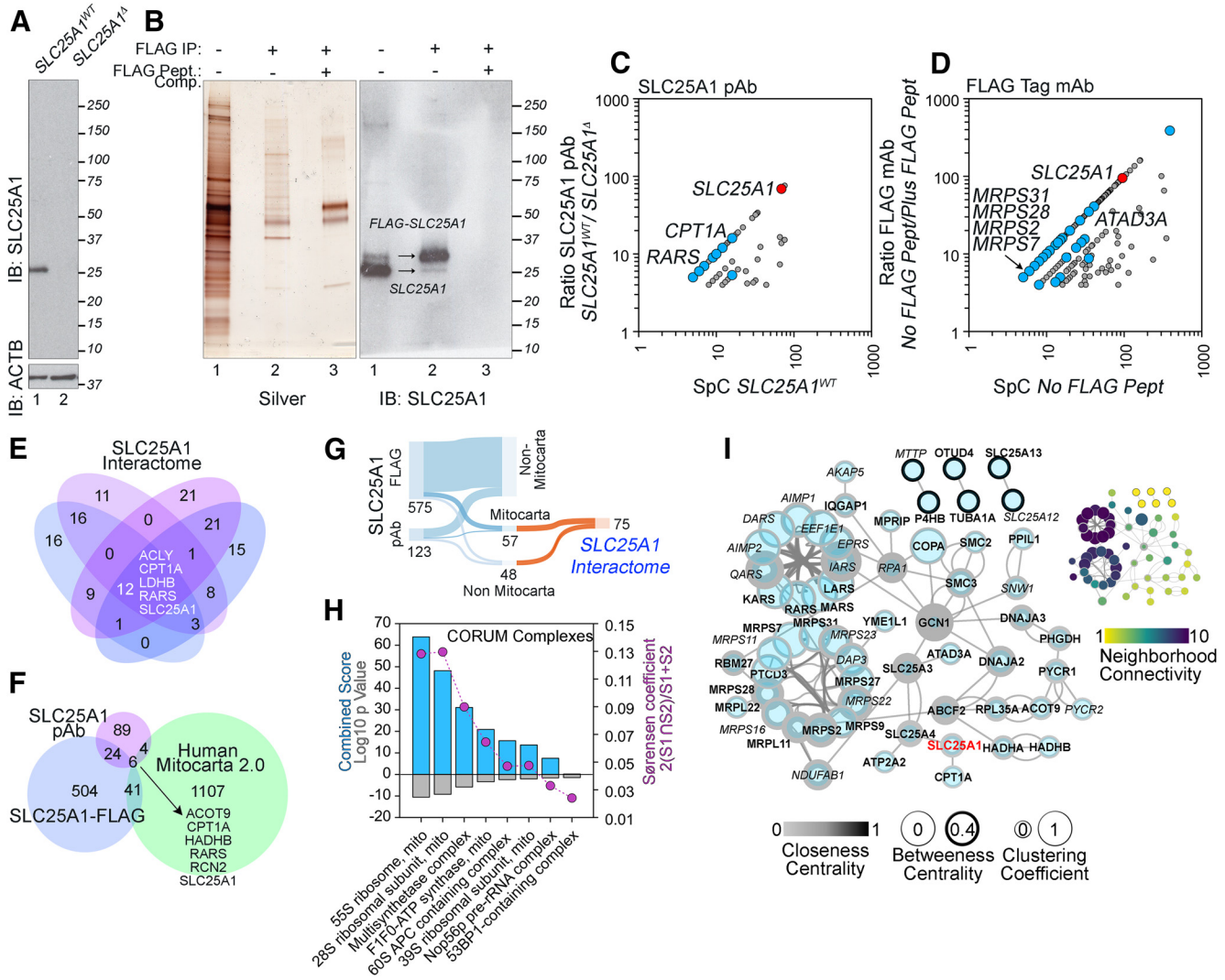

Figure 1. The SLC25A1 mitochondrial interactome. ***A***, Immunoblot of SLC25A1 with WT and SLC25A1 null cell extracts. Loading control performed with actin (ACTB). ***B***, Immunoaffinity isolation of FLAG-SLC25A1 from stably expressing SH-SY5Y neuroblastoma cells. Panels represent silver-stained SDS-PAGE and its corresponding SLC25A1 immunoblot. Lane 1, Input. Lanes 2 and 3, FLAG peptide elution from magnetic beads. Lane 3, Outcompetition with excess FLAG peptide before FLAG peptide elution. ***C***, Spectral count (SpC) enrichment scatter plots for SLC25A1 interacting proteins. Proteins were isolated with a SLC25A1 antibody from WT and SLC25A1 null cell extracts. ***D***, Spectral count (SpC) enrichment scatter plots of SLC25A1 interacting proteins. Proteins were isolated with FLAG antibody from SH-SY5Y cell extracts in the absence or presence of FLAG peptide outcompetition. ***E***, Venn diagram represents all four individual proteomes giving rise to graph in ***C***. ***F***, Venn diagram describes overlaps between the proteomes depicted in ***C*** and ***D*** and the Mitocarta 2.0 dataset. ***G***, Sankey graph represents the selection of the SLC25A1 mitochondrial interactome starting from the proteomes in ***C*** and ***D***. ***H***, CORUM complexome analysis of the SLC25A1 mitochondrial interactome. Y1, Log *p* value (Fisher Exact Test) and the combined score (log *p* value × *Z* score); Y2, Sørensen commonality index between the SLC25A1 mitochondrial interactome and curated protein complexes. ***I***, *In silico* network of the SLC25A1 mitochondrial interactome analyzed by graph theory with Cytoscape to identify nodes of high connectivity and subnetworks. Proteomics data are available in Extended Data Figures 1-2 and 1-3. For SLC25A1 antibody further characterization, see Extended Data Figure 1-1.

were selectively bound to FLAG beads (Fig. 1*D*,*F*; Extended Data Fig. 1-3). Overall, these five pulldown experiments converged in 30 common proteins, 6 of which were mitochondrial proteins, including SLC25A1 (Fig. 1*F*, 24 + 6; Fig. 1*G*). Of all proteins that co-isolated with SLC25A1, 51 of them intersected with the Mitocarta 2.0 proteome (Fig. 1*F*, 41 + 6 + 4; Fig. 1*G*). In total, 75 SLC25A1 interacting proteins were selected from proteins common to all five pulldown experiments plus the Mitocarta curated SLC25A1 proteins (Fig. 1*F*, 24 + 6 + 41 + 4; Fig. 1*G*). These 75 proteins are henceforth referred as the SLC25A1 mitochondrial interactome (Fig. 1*G*).

We analyzed the SLC25A1 mitochondrial interactome with several orthogonal bioinformatic tools and databases to unbiasedly identify and prioritize molecular mechanisms and protein complexes enriched in this dataset (Fig. 1*H*,*I*). We interrogated the CORUM complex database to determine what molecular complexes were preferentially enriched among the SLC25A1 interacting proteins (Fig. 1*H*) (Giurgiu et al., 2019). The SLC25A1 mitochondrial interactome was enriched in subunits of the small and large mitochondrial ribosome subunits, 17 in total (Sørensen index of 0.18; Fig. 1*H*). In addition, we found 4 mitochondrial aminoacyl t-RNA synthetases and 3 subunits of the mitochondrial ATPase or complex V (Fig. 1*H*). Graph connectivity analysis revealed that mitochondrial protein synthesis, in the form of mitochondrial ribosomes and aminoacyl tRNA synthetases, is a high connectivity subnetwork embedded within the SLC25A1 mitochondrial interactome (Fig. 1*I*). These bioinformatic findings argue that SLC25A1 functionally interacts with the mitochondrial protein synthesis machinery.

SLC25A1 interacts and cofractionates with MRPL40 and other subunits of the mitochondrial ribosome

The association of SLC25A1 with the mitochondrial protein synthesis machinery (Fig. 1*H*,*I*) prompted us to directly test whether the mitochondrial ribosome subunit MRPL40, which is encoded in the 22q11.2 microdeleted segment, is associated with SLC25A1. We expressed MRPL40-FLAG in SH-SY5Y neuroblastoma cells and asked whether endogenous SLC25A1 and recombinant MRPL40-FLAG colocalized and coimmunoprecipitated (Fig. 2*A*,*C*). First, we validated the SLC25A1 antibody by performing stainings in differentiated neuroblastoma cells where we mutagenized the SLC25A1 locus by CRISPR-Cas9 genome editing (Extended Data Fig. 1-1*A*-*C*). SLC25A1 colocalized with the mitochondrial marker TOMM20 in WT cells, but the SLC25A1 fluorescent signal was absent in SLC25A1-null cells (Extended Data Fig. 1-1*C*). SLC25A1 strongly colocalized with transfected MRPL40 both in cell bodies of both differentiated WT neuroblastoma cells (Fig. 2*A*) as well as primary hippocampal neurons in culture (Fig. 2*B*). Transfected MRPL40-FLAG immunoprecipitated SLC25A1 and the mitochondrial ribosome subunit MRPL11, a subunit adjacent to MRPL40 in the 39S ribosome structure (Fig. 2*C*, Lane 5) (Koripella et al., 2019). The specificity of these coprecipitations was determined by the absence of bands in blots from nontransfected cell precipitations (Fig. 2*C*, Lane 3) and by outcompeting SLC25A1 and MRPL11 with an excess of FLAG peptide during FLAG precipitations (Fig. 2*C*, Lane 6). We confirmed these findings in mouse brain cortex homogenates by coprecipitating endogenous SLC25A1 and MRPL40 with antibodies against MRPL40 (Fig. 2*D*). Selective binding of mouse brain SLC25A1 to MRPL40 antibody beads was twice above nonspecific signal (Fig. 2*D*, Lane 1 compare with Lanes 2 and 3). We measured this nonspecific signal in immunoprecipitations performed with beads alone (Fig. 2*D*, Lane 2) or by outcompeting coprecipitating SLC25A1 with an excess of purified recombinant 6-His::MRPL40 during MRPL40 precipitations (Fig. 2*D*, Lane 3). These results indicate that two mitochondrial proteins encoded in the 22q11.2 microdeleted syndrome biochemically associate.

We further examined the interactions between SLC25A1 and the mitochondrial ribosome performing immunoprecipitations from FLAG-tagged SLC25A1-expressing SH-SY5Y neuroblastoma cells with antibodies against other mitochondrial ribosome subunits (Fig. 2*E*,*F*,*H*). Antibodies against any of the mitochondrial ribosome subunits MRPL11, MRPL14, or MRPL52 precipitated FLAG-SLC25A1 (Fig. 2*E*,*F*,*H*, Lane 2). We controlled for the selectivity of these associations with beads decorated with a control antibody (Fig. 2*E*,*F*,*H*, compare Lanes 2 and 3). In addition, reciprocal immunoprecipitations of FLAG-SLC25A1 brought down MRPL11, an association outcompeted with excess FLAG peptide (Fig. 2*G*, compare Lanes 2 and 3). These biochemical studies demonstrate that SLC25A1 interacts with components of the mitochondrial ribosome, including MRPL40.

If SLC25A1 and MRPL40 coprecipitate from brain detergent homogenates, then SLC25A1 and MRPL40 should cofractionate in neuronal compartment where mitochondria reside, such as cell bodies and synapses. To test this idea, we first assessed the distribution of SLC25A1 in primary hippocampal neurons in culture by immunomicroscopy (Extended Data Fig. 2-2*A*). SLC25A1 together with the vital mitochondrial dye MitoTracker localized preferentially to neuronal cell bodies, suggesting that the majority of SLC25A1-positive mitochondria would fractionate in low-speed fractions (Fig. 2*B*; Extended Data Fig. 2-2*A*). We fractionated adult mouse cortex by differential centrifugation followed by Percoll-density sedimentation of high-speed P2 pellets (Extended Data Fig. 2-2*B*) to obtain fractions enriched in synaptosomes and mitochondria (Extended Data Fig. 2-2*B*) (Nagy and Delgado-Escueta, 1984). As predicted by SLC25A1 immunomicroscopy, the majority of SLC25A1 and its interacting MRPL40 were found in low-speed sedimenting fractions (Extended Data Fig. 2-2*C*, fraction P1 compared with homogenate, Hom, and P2). Importantly, the majority of SLC25A1 and MRPL40 present in the high-speed P2 pellet cosedimented with Percoll fractions enriched in synapses, detected with the synaptic vesicle protein SV2 (Extended Data Fig. 2-2*C*, heavy synaptosomes [HS]), and mitochondria (Extended Data Fig. 2-2*C*, Mito). Because of the low MRPL40 and SLC25A1 immunoblot signal in some of these mouse brain fractions, we confirmed the presence and enrichment of MRPL40 and SLC25A1 in Percoll heavy synaptosomes and mitochondria by label-free quantitative mass spectrometry (Extended Data Fig. 2-2*E*, dotted lines). These findings agree with the results of Maynard et al. (2008) who first described the presence of MRPL40 in synaptic fractions.

To determine whether SLC25A1 associated with MRPL40 as part of mitochondrial ribosomes or as free MRPL40 polypeptide, we solubilized brain Percoll-isolated mitochondria in a high-magnesium detergent buffer to further resolve high-molecular weight mitochondrial complexes in magnesium-rich sucrose gradients (Extended Data Fig. 2-2*B*). Under these conditions, mitochondrial ribosomes and associated proteins are stabilized migrating at the bottom of these gradients (Matthews et al., 1982). A small amount of SLC25A1 cosedimented with MRPL40 present in intact mitochondrial ribosomes at the bottom of magnesium-rich sucrose gradients (Extended Data Fig. 2-2*D*), a finding that we confirmed by mass spectrometry of the heaviest sucrose fractions (Extended Data Fig. 2-2*E*). These results demonstrate that brain MRPL40-positive mitochondrial ribosomes associate with SLC25A1.

SLC25A1 genetic defects compromise mitochondrial ribosome integrity

Subunits of a protein complex are frequently downregulated after genetic elimination of one of the complex components (Mullin et al., 2011; Wu et al., 2013). Therefore, we reasoned that ablation of SLC25A1 should alter the expression of mitochondrial ribosome subunits if the transporter and the ribosome were to interact. We tested this idea genetically in two CRISPR-Cas9 SLC25A1 null clones to exclude off-target CRISPR-Cas9 effects. We comprehensively quantified the expression of mitochondrial ribosome protein subunits using TMT mass spectrometry (Werner et al., 2012). We quantified 77 of the 78 CORUM annotated mitochondrial ribosome subunits (CORUM complex ID:320, Fig. 2*I*). Expression of 56 mitochondrial ribosome subunits (73%) was decreased in both null SLC25A1 clones, including MRPL40 (Fig. 2*I*). In contrast, the expression of the 74 subunits of the cytoplasmic ribosome measured by TMT mass spectrometry did not show differences that clustered according to cell genotype (CORUM complex ID:306, Fig. 2*I*). We confirmed reduced expression of small and large mitochondrial ribosome subunit proteins by immunoblot and qRT-PCR expression analysis in both SLC25A1 null clones (Fig. 2*J*,*K*). These results demonstrate that SLC25A1 biochemically and genetically interacts with the mitochondrial ribosome.

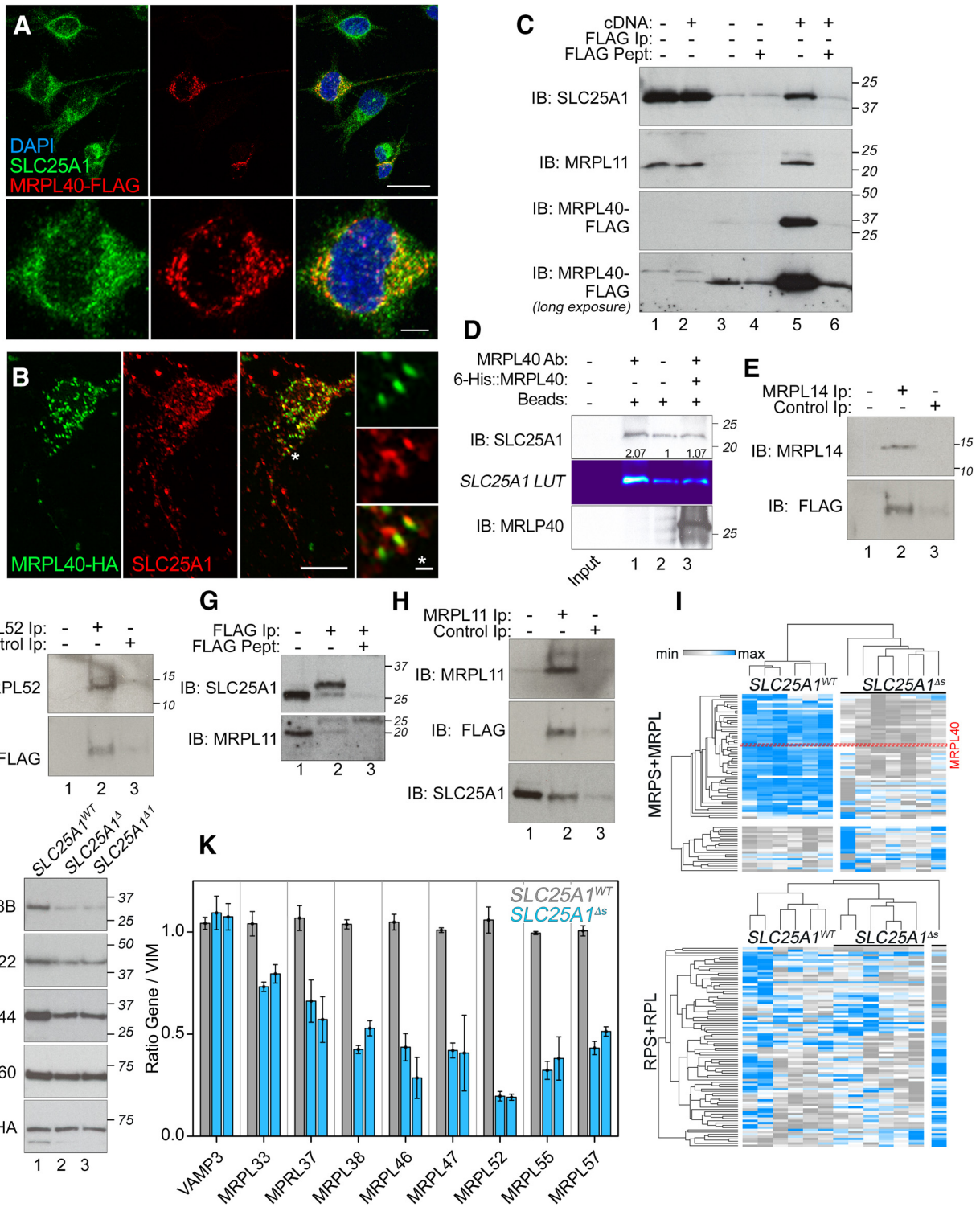

Figure 2. SLC25A1 interacts with MRPL40 and other mitochondrial ribosome proteins. ***A***, Colocalization of SLC25A1 and transfected MRPL40-FLAG in differentiated SH-SY5Y neuroblastoma cells. Images correspond to a *Z*-stack projection. Calibration bars: 25 μm, 5 μm. ***B***, Primary hippocampal neurons transfected with MRPL40-HA and immunostained with SLC25A1 and HA antibodies. Images represent a *Z*-stack projection. Calibration bars: 10 μm, 1 μm. ***C***, Detergent extracts from SH-SY5Y neuroblastoma cells, untransfected controls, and those expressing MRPL40-FLAG immunoprecipitated with antibodies against the FLAG tag followed by immunoblot with antibodies against endogenous SLC25A1 or MRPL11. Lanes 1 and 2 inputs, Lanes 3 and 4 non-transfected cell controls. Lanes 4 and 6, Controls with FLAG peptide outcompetition. ***D***, Immunoprecipitation from detergent extracts mouse brain cortex P1 fractions (Extended Data Figure 2-2*B*) with antibodies against MRPL40 followed by immunoblot with antibodies against endogenous SLC25A1 or MRPL40. Lanes 2 and 3, Nonspecific controls of beads alone or outcompetition with bacterially produced 6His::MRPL40, respectively. Numbers in lanes indicate the band intensity determined with Fiji. ***E***, ***F***, ***H***, Immunoprecipitations from detergent extracts of SH-SY5Y neuroblastoma cells expressing FLAG-SLC25A1 with antibodies against MPRL11, MRPL14, and MRPL52 were immunoblotted with FLAG tag antibodies to detect recombinant FLAG-SLC25A1. Lane 1, Inputs. Lane 3, Controls with HA antibodies. ***G***, Detergent extracts from SH-SY5Y neuroblastoma cells expressing FLAG-SLC25A1 immunoprecipitated with antibodies against the FLAG tag and blotted with MRPL11 antibodies. Lane 3, Control with FLAG peptide excess. For SLC25A1 antibody characterization, see Extended Data Figure 1-1. ***I***, TMT quantification of mitochondrial (MRPL and MRPS) and cytosolic ribosome subunits (RPL and RPS) in WT and two SLC25A1 null clones; $n = 6$. Clustering was performed with average linkage for columns and rows with One minus Pearson correlation. ***J***, Immunoblots of WT and SLC25A1 null cells probed with mitochondrial ribosome subunits (MRPS18B, MRPS22, and MRPL44) and two loading control mitochondrial

The extensively downregulated expression of small and large mitochondrial ribosome subunit proteins observed in SLC25A1 null cells suggests a defect in the integrity of the mitochondrial ribosome. We determined the integrity of mitochondrial ribosomes fractionating detergent-soluble extracts from WT and SLC25A1 null cells in high magnesium sucrose media. We selected high magnesium media because it stabilizes the mitochondrial ribosome (Matthews et al., 1982). Silver stain of equilibrium magnesium-sucrose fractions showed differences in the protein profile in the high molecular weight/sedimentation fractions (Fig. 3*A*, Lanes 1 and 2, compare WT and SLC25A1 null). Immunoblots revealed that the magnesium-sucrose fraction 1 contained SLC25A1 (Fig. 3*A*, Lane 1) and proteins of the small and large ribosome subunits, MRPS18B and MRPL44, respectively (Fig. 3*B*, Lanes 1 and 2). Importantly, the sedimentation of MRPS18B and MRPL44 shifted to lighter fractions in SLC25A1 null cells. We observed a drastic reduction in the content of MRPS18B and MRPL44 sedimenting in the heaviest fraction of the gradient (Fig. 3*B*, Lanes 1 and 2). The decreased sedimentation of mitochondrial ribosome subunits was selective as the cytoplasmic ribosome sucrose sedimentation was not affected in SLC25A1 null cells (Extended Data Fig. 3-1).

We confirmed that sucrose fraction 1 enriched mitochondrial ribosomes by performing label-free quantitative mass spectrometry in WT and null cells. We identified 1140 proteins in fraction 1 (Fig. 3*C*,*D*; Extended Data Fig. 3-2). Among these proteins, 192 reside in mitochondria according to Mitocarta 2.0, and 34 were common with the SLC25A1 mitochondrial interactome defined in Figure 1*G* (see also Fig. 3*C*). The mitochondrial proteins in fraction 1 include all the subunits of the mitochondrial ribosome (Sørensen index of 0.98; Fig. 3*E*), 3 aminoacyl tRNA synthetases (Sørensen index of 0.18; Fig. 3*E*), 3 proteins required for the assembly of mitochondrial ribosomes (DDX28, DHX30, and FASTKD2), mitochondrial elongation factor and RNA polymerase (MTIF2 and POLRMT), and 9 SLC25A transporters, including SLC25A1 (Fig. 3*A*,*C*,*E*) (Antonicka and Shoubridge, 2015; Arroyo et al., 2016). These 192 mitochondrial proteins were absent or reduced more than twofold in fraction 1 from SLC25A1 null cells (Fig. 3*D*, blue symbols). In contrast, we found 40 proteins whose content in fraction 1 remained unchanged regardless of the genotype. These proteins include actin, vimentin, and cytoplasmic snRNP subunits (see ACTB and VIM as well as Fig. 3*D*, purple symbols). Importantly, 162 of these 192 proteins sensitive to SLC25A1 mutations in cultured cell lines were also present in identical heavy sucrose fractions enriched in brain mitochondrial ribosomes (Extended Data Figs. 2-2*F*,*G* and 3-2). These results demonstrate that associations of mitochondrial ribosomes with nonribosomal mitochondria proteins, such as SLC25A1, are shared between cell lines in culture and brain.

We further probed mitochondrial ribosome integrity by measuring the expression of the mitochondria genome-encoded 12S and 16S ribosomal RNAs (MTRNR1 and MTRNR2). Expression of both mitochondrial rRNAs decreased to ~25% of WT levels in mutant cells (Fig. 3*F*). This rRNA phenotype is not attributable to decreased number of mitochondrial genomes per nuclear genome in SLC25A1 null cells. Indeed, null cells had an increase of ~2.5-fold in the number of mitochondrial genomes (Fig. 3*G*). The selectivity of this change was determined by measuring mitochondrial genome dosage in $\rho 0$ DU145 cells, which lack mitochondrial DNA (Fig. 3*G*) (Marullo et al., 2013). These results demonstrate that the integrity of the mitochondrial ribosome requires the expression of SLC25A1.

A downstream consequence of decreased mitochondrial ribosome integrity is reduced expression of the 13 proteins encoded by the mitochondrial genome. The translation of these proteins requires the mitochondrial ribosome (Taanman, 1999; Wallace, 2010; Couvillion et al., 2016). TMT proteomics of control and SLC25A1 null cells detected 8 of the 13 mitochondrially encoded proteins. These 8 mitochondrially encoded proteins were expressed at lower levels in SLC25A1 null cells compared with controls (Fig. 3*H*). We confirmed these mass spectrometry findings by immunoblot with antibodies against the cytochrome C oxidase complex/complex IV subunits MT-CO1 and MT-CO_2 (Fig. 3*I*). The reduced content of assembled mitochondrial ribosomes plus the decreased expression of mitochondrially expressed proteins strongly argue that mitochondrial proteostasis is impaired in SLC25A1 mutant cells.

SLC25A1 deficiency increases the sensitivity to agents that disrupt mitochondrial proteostasis

We probed the susceptibility of WT and both SLC25A1 mutant clones to drugs that disrupt mitochondrial proteostasis. We used agents that either inhibit mitochondrial protein synthesis or that impair mitochondrial protein quality control mechanisms. Mitochondrial oxygen consumption rates were measured with Seahorse technology in the absence or presence of these drugs. We selected mitochondrial protein synthesis inhibitors that differ in their chemistries and mechanisms to halt mitochondrial translation (doxycycline, minocycline, chloramphenicol, and linezolid) (Skrtic et al., 2011; Wilson, 2014; Chatzispyrou et al., 2015; Moullan et al., 2015). Mitochondrial protein quality control was impaired with actinonin, a drug that induces mitochondrial proteotoxicity (Richter et al., 2015; Burman et al., 2017). Furthermore, actinonin stalls mitochondrial ribosomes triggering mitochondrial ribosome and RNA downregulation (Richter et al., 2013).

Control cells incubated up to 5 d with 2.25 μM doxycycline did not experience significant modifications in the basal or stress-induced rates of oxygen consumption (Fig. 4*A*). In contrast, the same dose of doxycycline elicited a progressive decline in mitochondrial respiration in SLC25A1 null cells over time (Fig. 4*A*, blue symbols). Increasing doxycycline concentrations preferentially affected mitochondrial respiration parameters in mutant cells. Doxycycline compromised basal respiration (Fig. 4*B*,*E*), the respiration dependent on the activity of the mitochondrial ATPase (Fig. 4*C*), and the respiration elicited by mitochondrial protonophores, the latter an indication of the mitochondrial respiratory reserve (Fig. 4*D*). The same results were obtained with minocycline, a structural analog of doxycycline, that shows promise in preclinical models for the treatment of neurodevelopmental disorders (Extended Data Fig. 4-1*A*) (Bilousova et al., 2009; Dziembowska et al., 2013; Garrido-Mesa et al., 2013; Giovanoli et al., 2016). WT cells were insensitive to low micromolar concentrations of diverse mitochondrial protein synthesis inhibitors, whereas under identical conditions SLC25A1-null cells were more sensitive to chloramphenicol and linezolid, two drugs structurally unrelated to

←

proteins (HSP60 and SDHA). ***K***, qRT-PCR quantitation of mitochondrial ribosome transcripts from WT and SLC25A1 null cells. Controls were performed measuring VAMP3 and VIM. All data expressed as a ratio with VIM ($n = 3$-6). VAMP3 expression is not significantly different between genotypes. All MRPL mRNAs are significantly reduced. Kruskal–Wallis Test ($p < 0.0001$) followed by two-tailed pairwise comparisons with Mann–Whitney *U* test (all *p* values between 0.0039 and 0.0495). A primers list can be found in Extended Data Figure 2-1. Fractionation data are available in Extended Data Figure 2-2.

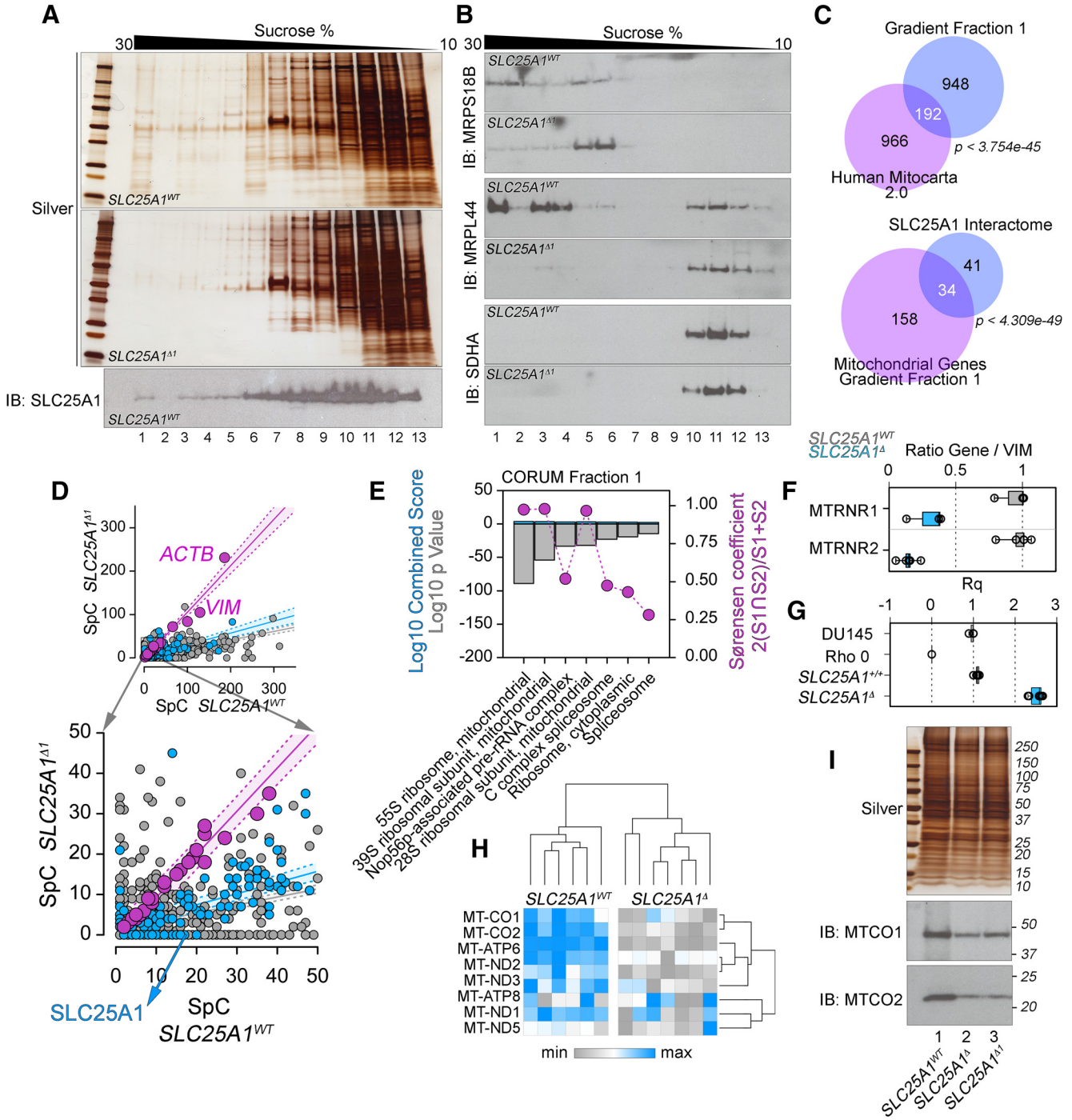

Figure 3. Mitochondrial ribosome integrity is compromised in SLC25A1 null cells. Detergent extracts from WT and SLC25A1 null cells were resolved in magnesium-sucrose gradients. Fractions were analyzed by SDS-PAGE followed by silver stain (***A***) or immunoblots (***B***) with antibodies against SLC25A1 (***A***) or mitochondrial ribosome subunits (MRPS18B and MRPL44). Controls were performed with SDHA antibodies. ***C***, Venn diagram describes overlaps between the proteome in fraction 1 and the Mitocarta 2.0 dataset or with the SLC25A1 mitochondrial interactome. *p* values determined by Exact Hypergeometric Probability Test. ***D***, Spectral count (SpC) scatter plots for fraction 1 proteome in WT and SLC25A1 mutant cells. Purple symbols represent proteins present in both WT and mutant fraction 1 at the same level (slope 1.06, $r = 0.978$). Gray symbols represent nonmitochondrial proteins enriched >2 fold in WT fraction 1 over mutant (slope 0.19, $r = 0.591$). Blue symbols represent mitochondrial proteins enriched >2 fold in WT fraction 1 (slope 0.27, $r = 0.699$). Belts represents 99% CI. ***E***, CORUM complexome analysis of WT fraction 1 proteome. Y1, Log 10 *p* value (Fisher's exact test) and the combined score (log *p* value × *Z* score); Y2, Sørensen commonality index between WT fraction 1 proteome and curated protein complexes. ***F***, qRT-PCR of mitochondrial ribosome RNAs expressed as a ratio to a control RNA (VIM). MTRNR1: $n = 3$, $p = 0.0495$; MTRNR2: $p = 0.009$, $n = 5$. ***G***, Ratio of mitochondrial and nuclear genomes per cell type (Rq). DU145 and $\rho 0$ cells: $p = 0.0495$, $n = 3$. WT and SLC25A1 null cells: $p = 0.0039$, $n = 6$. ***F***, ***G***, Two-tailed pairwise comparisons with Mann–Whitney *U* test. ***H***, TMT quantification of mitochondrial genome encoded proteins in WT and two SLC25A1 null clones; $n = 6$. Clustering was performed with average linkage for columns and rows with One minus Pearson correlation. ***I***, Immunoblots of WT and SLC25A1 null cell extracts probed with antibodies against MT-CO1 and MT-CO2. Silver SDS-PAGE was used as loading control. For complete hit list, see Extended Data Figure 3-2; see also Extended Data Figure 3-1.

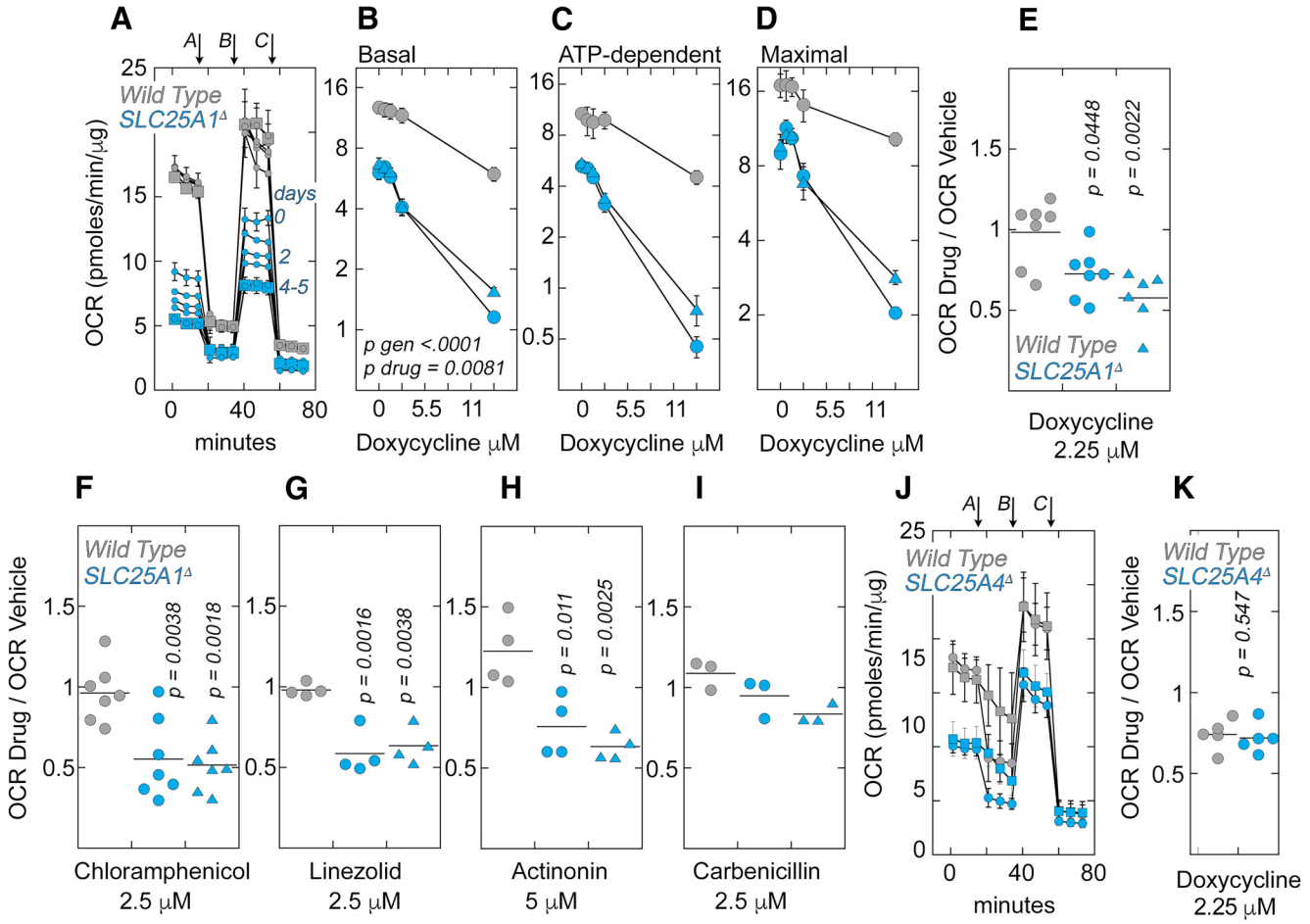

Figure 4. SLC25A1 genetic defects selectively confer susceptibility to mitochondrial proteostasis inhibitors. Mitochondrial oxygen consumption rate (OCR) was analyzed with Seahorse technology in WT and two clones of SLC25A1 null cells. Cells were incubated in the absence or presence of drugs that target mitochondrial protein synthesis (***A-G***) or mitochondrial protein quality control (***H***). Carbenicillin was used as a control drug (***I***, n = 3). All cells were treated for 48 h with drugs, except for ***A***. ***A***, Stress test after increasing incubation times with 2.25 μM doxycycline. Data are mean ± SD; $n = 8$. Arrows A-C indicate times of stress test drug injections: oligomycin, FCCP, and antimycin plus rotenone, respectively. ***B-D***, Basal, ATP-dependent, and maximal OCR of untreated and doxycycline-treated SLC25A1 null and WT cells. Data are mean ± SE; $n = 4$-6. ***E-I***, Normalized basal OCR of cells treated in the absence or presence of doxycycline, chloramphenicol, linezolid, or actinonin. Carbenicillin was used as a control antibiotic. Data are mean ± SE; $n = 4$-7. ***J***, Same as in ***A***, but WT and SLC25A4 null cells were treated for 48 h in the absence or presence of 2.25 μM doxycycline. ***K***, Normalized basal OCR ratios for drug-treated and untreated WT and SLC25A4 null cells. ***B-D***, *p* values were calculated with two-factor ANOVA with repeated measures. ***E-I***, ***K***, *p* values were calculated by one-way ANOVA followed by multiple-comparison correction by the Bonferroni method. Gray and blue symbols represent WT and mutants, respectively. See Extended Data Figure 4-1.

tetracycline derivatives, that prevent mitochondrial protein synthesis by distinct mechanisms (Skrtic et al., 2011; Wilson, 2014; Chatzispyrou et al., 2015; Moullan et al., 2015) (Fig. 4*F*,*G*; Extended Data Fig. 4-1*B*). This increased sensitivity to mitochondrial protein synthesis inhibitors observed in SLC25A1 mutants was also elicited by actinonin, an agent that impairs mitochondrial protein quality control (Fig. 4H; Extended Data Fig. 4-1*B*).

We used three approaches to assert drug specificity and genotype selectivity of these chemical perturbations of mitochondrial proteostasis. First, we incubated cells with carbenicillin, a β lactamic antibiotic that spares prokaryotic and mitochondrial ribosomes yet elicits similar oxidative stress responses as tetracycline in mammalian cells (Drawz and Bonomo, 2010; Kalghatgi et al., 2013). Both WT and SLC25A1 mutant cells were resistant to carbenicillin (Fig. 4*I*). Second, we tested genotype selectivity with an isogenic mutant line where the mitochondrial ADP-ATP transporter, SLC25A4, was removed by CRISPR gene editing. Mitochondrial respiration in SLC25A4 mutant cells was impaired in basal and stress-induced conditions to a similar extent as SLC25A1 mutant cells (Fig. 4*J*). However, even when mitochondrial function was compromised in SLC25A4 cells, they remained unaffected by doxycycline at concentrations that affected SLC25A1 mutants (Fig. 4*J*,*K*). Finally, we used WT DU145 cells and a DU145 variant cell line lacking mitochondrial genome, $\rho 0$ cells, to test whether the effects of tetracycline derivatives require intact mitochondria and their ribosomes. The viability of WT cells was decreased by increasing concentrations of doxycycline while $\rho 0$ cells were resistant up to 11.25 μM doxycycline (Extended Data Fig. 4-1*C*). This concentration of doxycycline was able to reduce mitochondrial respiration by 50% in WT DU145 cells (Extended Data Fig. 4-1*D*). However, the lack of oxygen consumption in $\rho 0$ cells observed in the absence of drug remained steady at all doxycycline concentrations tested. This finding excludes extramitochondrial oxygen consumption elicited by off-target effects of this antibiotic (Extended Data Fig. 4-1*E*). We conclude that the effects of antibiotics targeting mitochondrial ribosome protein synthesis and quality control are drug-selective and genotype-specific. Moreover, these effects are independent of compromises in mitochondrial respiration, as indicated by SLC25A4 null cells and $\rho 0$ cells. These studies functionally demonstrate that SLC25A1 ablation/deficiency selectively compromise mitochondrial proteostasis.

Mitochondrial ribosome subunit expression is developmentally and anatomically regulated in human brain

We analyzed the mitochondrial ribosome's potential to contribute to neurodevelopment in normal and disease states by analyzing the ontology and anatomy of mitochondrial ribosome gene expression in brain. We reasoned that expression changes in critical neurodevelopmental periods, regional differences in expression, and/or cell type specific patterns of mitochondrial ribosome gene expression would affirm a neurodevelopmental potential for the mitochondrial ribosome. We used two independent databases that assess mRNA expression across brain regions and lifespan, BrainSpan and the Evodevoapp (Hawrylycz et al., 2012; Miller et al., 2014; Cardoso-Moreira et al., 2019). Brain expression of all mitochondrial ribosome genes was developmental regulated (Fig. 5*A*). Some subunits were preferentially expressed during prenatal development, while a second group of mitochondrial ribosome genes were expressed at higher levels for a discrete period after birth and before adolescence (Fig. 5*A*; Extended Data Fig. 5-1). There were distinctive anatomic expression profiles at most ages in the human brain (Extended Data Fig. 5-1). We confirmed ontological differences with the Evodevoapp dataset where we also found an increase in mitochondrial ribosome gene expression between birth and adolescence (Fig. 5*B*).

Emergence of the clinical features of neurodevelopmental disorders has been attributed to imbalances in excitation and inhibitory neuronal signaling (Rubenstein and Merzenich, 2003; Yizhar et al., 2011; Lewis et al., 2012; Nelson and Valakh, 2015). We sought to determine whether excitatory (glutamatergic) and inhibitory (parvalbumin-positive GABAergic) neurons differ in their mitochondrial ribosome gene expression in normal and disease states. We interrogated single-cell transcriptomic datasets from mouse adult cortex (Tasic et al., 2018). Of all cell types analyzed, parvalbumin-positive interneurons segregated away from other brain cell types, including pyramidal neurons from different cortical layers as revealed by linear and nonlinear data dimensionality reduction analysis, PCI and *t*-distributed stochastic neighbor embedding, respectively (Fig. 5*C*,*D*). These differences were driven by significantly higher levels of mitochondrial ribosome subunit mRNA expression in parvalbumin-positive interneurons (Fig. 5*E*). Second, we asked whether the expression of mitochondrial ribosome subunits was affected in schizophrenia, a neurodevelopmental disorder (Lewis and Levitt, 2002) highly prevalent in individuals with 22q11.2 microdeletion syndrome (Jonas et al., 2014; Guna et al., 2015; McDonald-McGinn et al., 2015). We analyzed transcriptomic datasets from dorsolateral PFC gray matter and three key circuit components, excitatory pyramidal neurons from cortical layers 3 and 5 and inhibitory parvalbumin interneurons from layer 3, in subjects with schizophrenia relative to unaffected comparison subjects (Fig. 5*F–J*) (Arion et al., 2015, 2017; Hoftman et al., 2015; Enwright et al., 2018). In dorsolateral PFC total gray matter, 18% of the CORUM-curated mitochondrial ribosome subunit genes were differentially expressed with lower levels in schizophrenia relative to unaffected comparison subjects (Fig. 5*J*). Nearly 30% of the mitochondrial ribosome subunit genes were differentially expressed with lower levels in layer 3 and layer 5 pyramidal excitatory neurons from schizophrenia subjects (Fig. 5*G*,*I*). Seven of these downregulated mitochondrial ribosome genes were shared between pyramidal neurons from layers 3 and 5 in schizophrenia subjects (Fig. 5*J*). In contrast with pyramidal neurons, only ~4% of mitochondrial ribosome subunit genes were differentially expressed in layer 3 parvalbumin interneurons from the same schizophrenia subjects (Fig. 5*H*). The sevenfold difference in the number of differentially expressed genes in schizophrenia between layer 3 parvalbumin neurons and layers 3 and 5 pyramidal neurons was significant ($p = 0.000358$ and $p = 0.000198$, respectively; Fisher Exact Probability Test). These results indicate that schizophrenia is associated with lower transcript levels of mitochondrial ribosome subunits in dorsolateral PFC gray matter, and this disease effect is more prominent in excitatory pyramidal neurons relative to inhibitory parvalbumin interneurons. These findings support the concept that the mitochondrial ribosome is a brain region and cell type-specific, neurodevelopmentally regulated organelle whose expression is disrupted in a neurodevelopmental disorder, such as schizophrenia.

Mitochondrial ribosome subunits are necessary for synapse neurodevelopment and behavior

We asked whether mitochondrial ribosomes are required for synapse development in the *Drosophila* larval neuromuscular junction. This is a validated synapse to assess phenotypes and mechanisms of human neurodevelopmental genetic disorders (Bier, 2005; Gatto and Broadie, 2011; Menon et al., 2013; Iyer et al., 2018). We previously demonstrated that genetic defects affecting the expression of the *Drosophila* citrate transporter SLC25A1, *scheggia* (*sea*, FBgn0037912), increase branching of the neuromuscular synapse at muscle VI-VII (Gokhale et al., 2019). We used this synapse preparation to assess phenotypes and genetic interactions after disruption of *sea* and two mitochondrial ribosome subunits, *mRpL15* and *mRpL40* (FBgn0036990 and FBgn0037892; Fig. 6). *mRpL15* and *mRpL40* are orthologs of human MRPL15 and the 22q11.2 encoded MRPL40 gene, respectively. We quantified synapse bouton numbers and branch size in animals where we selectively downregulated *sea*, *mRpL15*, or *mRpL40* in neurons (Fig. 6*A*). Downregulation was achieved with UAS-RNAi transgenes expressed from the neuronal-specific GAL4 driver *elav-c155* (Fig. 6) or a systemic actin-GAL4 driver to assess mRNA expression (Extended Data Fig. 6-1). Downregulation of each one of these three genes increased the complexity of the synapses as determined by increased number of synaptic boutons and total branch length per synapse (Fig. 6*A–D*). These synaptic phenotypes were similar regardless of whether RNAi was done just for a single gene or RNAi was performed simultaneously for *sea* plus an *mRpL* gene (Fig. 6*A–D*). We observed a similar synaptic phenotype after simultaneous RNAi for *mRpL15* and *mRpL40* RNAi (Fig. 6*A–D*). The increased morphologic complexity of *mRpL*-deficient synapses correlated with changes in synaptic function. The amplitude of evoked excitatory junctional potentials was increased after downregulation of either *mRpL15* or *mRpL40* with neuronal-specific RNAi, an observation in concordance with the increased number of boutons (Fig. 6*E*,*F*, EJP). Controls with either *UAS-RNAi* or *elav-C155* transgene alone were similar to WT *CS* synapses (Fig. 6*E*,*F*). We did not observe changes in the amplitude or frequency of spontaneous fusion events in any of these genotypes (Fig. 6*E*,*F*). We conclude that the *Drosophila* mitochondrial citrate transporter (*dSLC25A1* or *sea*) and mitochondrial ribosome subunits (*mRpL15*, *mRpL40*) reside on a common genetic pathway necessary for synapse development and function.

To determine the consequences of mitochondrial ribosome dysfunction on adult behavior, we measured *Drosophila* activity and sleep with the *Drosophila* Activity Monitor assay after

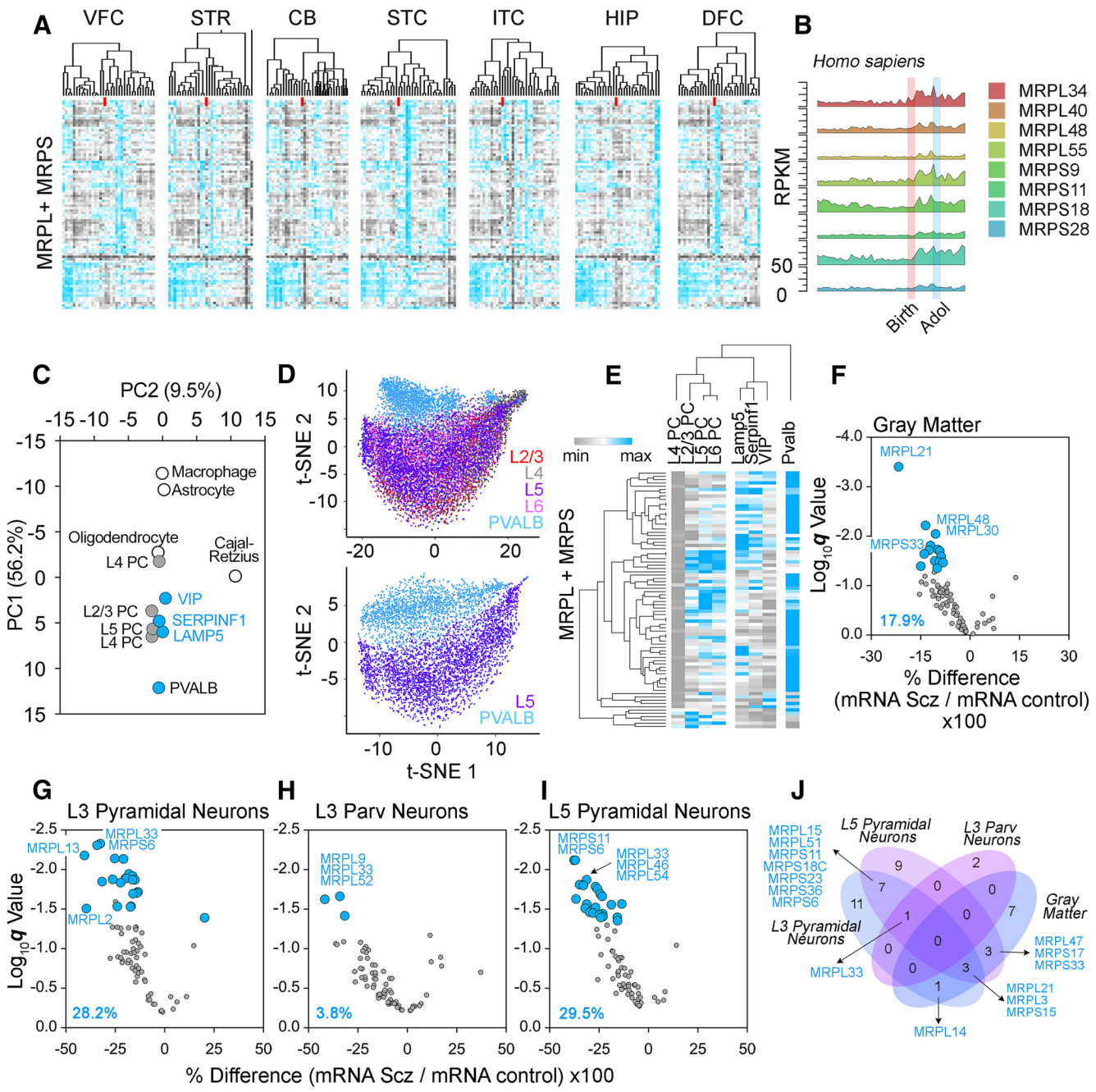

Figure 5. The mitochondrial ribosome is an anatomically and neurodevelopmentally regulated organelle. ***A***, Brain span expression of human mitochondrial ribosome subunit mRNAs. Heat map was clustered using One minus Spearman rank correlation for columns and rows. Rows represent *Z* scores. Red line roughly indicates prenatal (left) and postnatal (right) human development. Brain regions represent ventrolateral PFC (VFC), striatum (STR), cerebellum (CB), posterior (caudal) superior temporal cortex (area 22c, STC), inferolateral temporal cortex (area TEv, area 20, ITC), hippocampal formation (HIP), and dorsolateral PFC (DFC). ***B***, Evodevoapp gene expression of selected mitochondrial ribosome genes in human. ***C-E***, Analysis of 19,500 sequenced cells in the V1 mouse cortex dataset (Tasic et al., 2018). ***C***, Principal component analysis of the mRNA expression of the 78 mitochondrial ribosome subunits per the indicated cell categories. Gray symbols represent cortical pyramidal neurons. Blue symbols represent GABAergic neuron types. ***D***, *t*-distributed stochastic neighbor embedding (t-SNE) analysis of pyramidal and parvalbumin-positive cells of the data in ***C***. ***E***, Kendall tau hierarchical clustering of neuronal types (columns) and the averaged expression of 78 mitochondrial ribosome subunits (rows). ***F-I***, Volcano plots of mitochondrial ribosome gene expression control in gray matter (***F***), single pyramidal cells (***G***,***I***), or single parvalbumin cells (***H***) isolated from dorsolateral PFC of unaffected and schizophrenia cases. Gray matter mRNA quantitations were performed by RNAseq in 57 age- and sex-matched pairs of schizophrenia and unaffected comparison subjects. Cell type-specific analyses were performed by collecting populations of pyramidal neurons and parvalbumin interneurons via laser capture microdissection followed by microarray analysis in 36 age- and sex-matched pairs. Gray dots represent mitochondrial ribosome genes whose expression did not significantly differ in schizophrenia relative to unaffected comparison subjects. Blue symbols represent significant changes. ***J***, Venn diagram of genes whose expression is significantly different in schizophrenia samples. See Extended Data Figure 5-1.

mRpL15 and *mRpL40* RNAi (Fig. 7). We chose drivers for catecholaminergic neurons, *Ddc-GAL4*, and glutamatergic neurons, *vglut-GAL4*, to express UAS-RNAi transgenes. These drivers are expressed throughout development from the larval and early embryonic stage, respectively (Landgraf et al., 2003; Mahr and Aberle, 2006). Decreased expression of *mRpL15* and *mRpL40* did not compromise animal motility during their wakeful periods as measured by the average number of beam breaks per minute, thus excluding overt motor phenotypes in these animals (Fig. 7*A*). Total sleep time across a 24 h period was decreased after

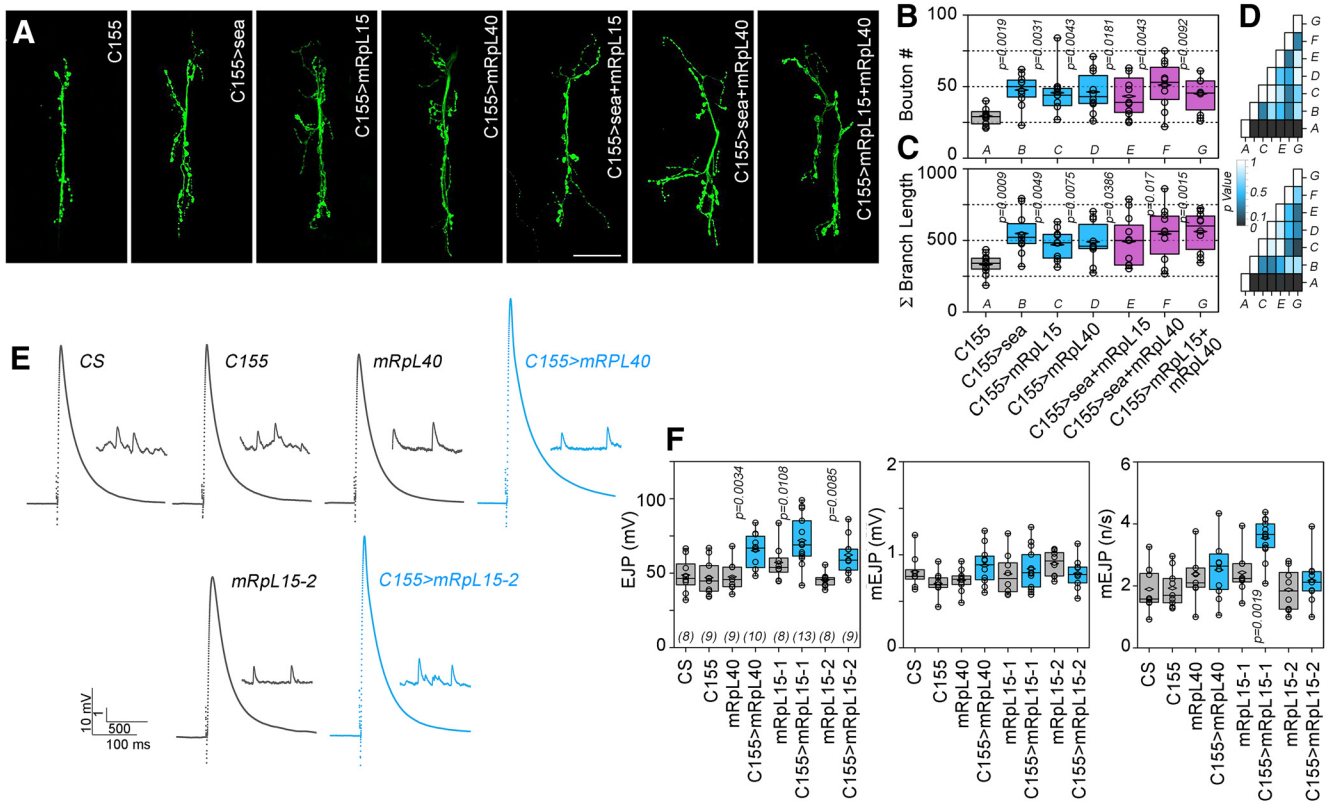

Figure 6. The mitochondrial ribosome is necessary for synapse development and function. ***A***, Muscle VI-VII neuromuscular junction preparations of third instar *Drosophila* larvae stained with HRP antibodies, which recognize a neuron-specific marker. ***B***, ***C***, Bouton counts per synapse and the total synapse processes length for animals raised on control food. ***D***, Heat map of *p* value comparisons of all genotypes analyzed for bouton number (upper map) and branch length (bottom map). Only row A (C155 Control) is significantly different compared with other genotypes. ***B***, ***C***, Actual *p* values. Kruskal–Wallis Test ($p = 0.0141$ for bouton numbers and $p = 0.0115$ for branch length) followed by two-tailed pairwise comparisons with Mann–Whitney *U* test; $n = 10$ or 11 animals per genotype. ***E***, Evoked (EJP) and spontaneous neurotransmission (mEJP) representative recordings from the third instar neuromuscular synapse on muscle VI-VII. Black traces represent Canton S (CS) and other controls. Blue traces represent synapse responses after downregulation of mRpL15 and mRpL40. ***F***, Box plots of EJP amplitude, mEJP amplitude, and mEJP frequency. Horizontal lines on box indicate the mean of the sample; diamond represents the median. *p* values were obtained with a one-way ANOVA followed by Bonferroni–Dunn Test. Values in parentheses are *n* values. See Extended Data Figure 6-1.

mRpL15 and *mRpL40* RNAi despite an increased number of sleep bouts (Fig. 7*B*,*C*). These sleep bouts were of shorter duration during both the 12 h light (day) and dark (night) periods in animals with disrupted mitochondrial ribosomes, thus accounting for the reduction in total sleep time (Fig. 7*D*,*E*). Phenotypes were not observed in control animals expressing just a GAL4 driver or a UAS-RNAi transgene (Fig. 7*B*–*E*). We interpret these findings as a sleep fragmentation phenotype, a common endophenotype in neurodevelopmental disorders (Robinson-Shelton and Malow, 2016). These results indicate that mitochondrial ribosome subunit expression from development to adulthood is necessary to sustain normal adult behavior.

Discussion

Synaptic development, function, and plasticity are under control of protein translation mechanisms that require cytoplasmic ribosomes and FMRP (Sutton and Schuman, 2006; Bassell and Warren, 2008). However, the participation of mitochondrial protein translation machinery in synaptic processes has not received the same level of scrutiny, with few exceptions, including the findings by Maynard et al. (Maynard et al., 2008; Devaraju et al., 2017; Akbergenov et al., 2018) who first identified MRPL40 in synaptic fractions. This dearth of information about mitochondrial protein synthesis and proteostasis in synapses is in stark contrast with the numerous human mutations affecting mitochondrial protein synthesis and degradation. These mutations associate with pathology, ranging from epileptic encephalopathy to neurodevelopmental and psychiatric disorders, which are also frequent phenotypes in mutations affecting bona fide synaptic genes (Shutt and Shadel, 2010; Wallace et al., 2010; Lightowlers et al., 2015; Lake et al., 2017; Akbergenov et al., 2018; Gardeitchik et al., 2018; Pei and Wallace, 2018; Nimmo et al., 2019). Here we make a case for mitochondrial ribosome integrity and proteostasis in synapse biology, focusing on genes encoded in a neurodevelopmental risk mutation, the 22q11.2 microdeletion syndrome locus.

We discovered a new function for SLC25A1 in mitochondrial proteostasis and its interaction with MRPL40. These two genes are encoded in the 22q11.2 microdeleted locus (Guna et al., 2015). SLC25A1 and mitochondrial ribosome subunits are necessary to sustain mitochondrial ribosome integrity, provide resistance to proteostasis disrupting drugs, and, in *Drosophila*, are required for synapse development, function, and normal sleep consolidation. We demonstrate the interaction between SLC25A1, MRPL40, and the mitochondrial ribosome by coprecipitation from cell lines, brain extracts, as well as by cofractionation of SLC25A1 and MRPL40 in brain synaptosomes, brain mitochondria, and brain mitochondrial ribosomes. Through the SLC25A1 mitochondrial interactome, we provide a broad view of SLC25A1 associations with the mitochondrial protein translation machinery (Fig. 1). These associations include multiple

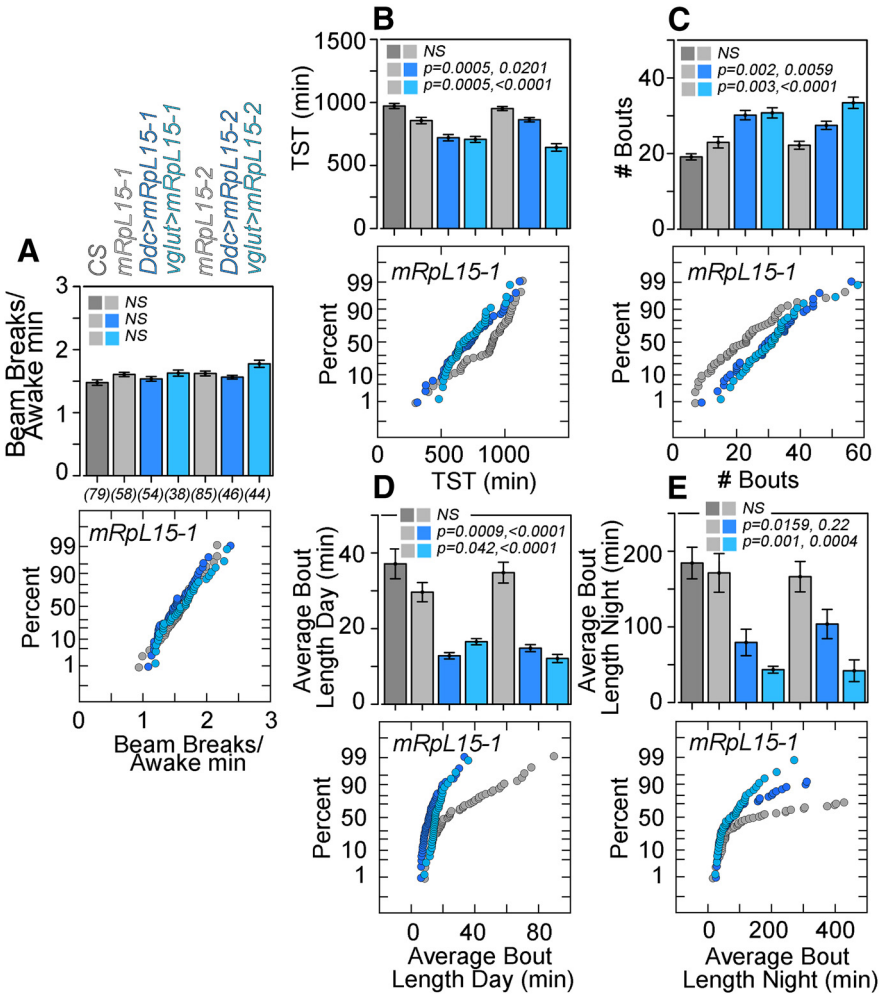

Figure 7. The mitochondrial ribosome is necessary for *Drosophila* behavior. *Drosophila* Activity Monitor assay results for Canton S (*CS*) and UAS-RNAi controls depicted in gray (*mRpL15-1* and *mRpL15-2*). Two RNAi strains were used to downregulate mRpL15 with the *Ddc-GAL4* or *vglut-GAL4* drivers (dark blue and light blue, respectively). ***A***, Average number of beam breaks per waking minute in a 24 h period, a measure of general locomotor activity, does not differ by genotype. ***B***, Total sleep time (TST) across a 24 h period is decreased with downregulation of mRpL15. ***C***, Total number of sleep bouts in a 24 h period is increased with downregulation of mRpL15. ***D***, ***E***, Average sleep bout duration during 12 h light period (day) or 12 h dark period (night), respectively, decrease with loss of mRpL15. Number of animals analyzed are presented in parentheses in ***A***. Data are graphed both as bar graphs (average ± SE) or as cumulative probability plots. *p* values were obtained with a one-way ANOVA followed by Bonferroni's comparison.

mitochondrial ribosome subunits and aminoacyl tRNA synthetases, a poly(A) polymerase (MTPAP), and proteins required for the assembly of mitochondrial ribosomes (DDX28, DHX30, and FASTKD2). Second, we confirmed the interaction between SLC25A1 and the mitochondrial ribosome and MRPL40 with reciprocal immunoprecipitations in cells in culture and brain (Fig. 2; Extended Data Fig. 2-2), cosedimentation of SLC25A1 and mitochondrial ribosome subunits in magnesium-sucrose gradients (Extended Data Fig. 2-2; Fig. 3), and, genetically, in human cells where the ablation of the SLC25A1 gene decreases the integrity of mitochondrial ribosomes and the expression of their subunits (Fig. 2). The consequential character of a reduced pool of mitochondrial ribosomes is demonstrated by three key observations in SLC25A1 mutants: (1) the decreased gene expression of respiratory chain genes encoded in the mitochondrial genome, which are strictly dependent on mitochondrial ribosomes for their translation (Fig. 3*H*, *I*); (2) decreased mitochondrial respiration in SLC25A1 mutant cells (Extended Data Fig. 1-1*D*; Fig. 4); and finally, (3) mutation of human SLC25A1 selectively conferred a heightened susceptibility to xenobiotic agents that either selectively inhibit mitochondrial protein translation (two tetracycline derivatives, chloramphenicol and linezolid) or impair mitochondrial protein quality control and ribosome stability (actinonin; Fig. 4). The concept that SLC25A1 and mitochondrial ribosomes belong to a common pathway is additionally supported by our genetic findings in *Drosophila* (Figs. 6 and 7). RNAi of SLC25A1, MRPL15, or MRPL40 fly orthologs phenocopy each other inducing an elaborated synapse phenotype at the neuromuscular junction (Fig. 6). These synaptic phenotypes are similar to those found in Fragile X mutant *Drosophila* (Zhang et al., 2001). Importantly, the magnitude of the SLC25A1 RNAi synaptic phenotype remains unchanged when concurrently decreasing mitochondrial protein synthesis by RNAi of mitochondrial ribosome subunits, thus indicating that SLC25A1 and the mitochondrial ribosome are part of a common pathway (Fig. 6). These results demonstrate a new and conserved requirement of SLC25A1 for mitochondrial protein translation and proteostasis.

We hypothesize that the absence of SLC25A1 compromises mitochondrial ribosome subunit expression by a combination of mechanisms. One mechanism considers that SLC25A1 stabilizes mitochondrial ribosomes or it is required for ribosome assembly through direct or indirect physical interactions, which are likely contained within the SLC25A1 mitochondrial interactome (Figs. 1 and 3) (Zeng et al., 2018). However, this model can only account for the reduced levels of mitochondrial ribosome proteins but not the concomitant reduction in mitochondrial ribosome mRNAs (Fig. 2*I*). The simultaneous downregulation in the expression of mitochondrial ribosome mRNAs and proteins needs additional models to be explicable. These models include the activation of the mitochondrial unfolded protein response by the absence of SLC25A1 as well as SLC25A1 mutant-dependent alterations in cell metabolism (Munch and Harper, 2016; Shpilka and Haynes, 2018). Mutations in SLC25A1 could reduce cytoplasmic levels of citrate and its product acetyl-CoA (Li et al., 2018; Majd et al., 2018). This metabolic model is supported by the interaction between SLC25A1 and ATP citrate lyase (ACLY), a key enzyme in the synthesis of acetyl-CoA from citrate (Fig. 1). Reduced levels of acetyl-CoA could influence gene expression by changing chromatin histone modifications or modifications in lipid metabolism (Wellen et al., 2009; Pietrocola et al., 2015; Srivatsan et al., 2020). We support the view that a convergence of these three mechanisms determines mitochondrial ribosome gene expression and integrity observed in SLC25A1 null cells. We consider these three potential mechanisms important in the

context of a neuron and its subcellular compartments. For example, local interactions between SLC25A1 and mitochondrial ribosomes could modulate mitochondrial protein translation and/or SLC25A1 transport function in selected synapses. Conversely, widespread metabolic modifications driven by changes in acetyl-CoA levels or the mitochondrial unfolded protein response could modify synapse function and neuronal excitability in a whole neuron. While our findings in *Drosophila* synapses do not discriminate between these models (Figs. 6 and 7), the *Drosophila* synapse and adult behavior phenotypes offer a genetically tractable experimental system where we can address this question.

Our findings demonstrate evolutionary conserved genetic and biochemical interactions between genes embedded within the 22q11.2 chromosomal locus. A recently proposed model to explain phenotypic pleotropism and overlap between different microdeletions is the idea that candidate genes within each microdeleted locus interact with each other through common pathways (Jensen and Girirajan, 2019). This model has received elegant experimental support through *Drosophila* genetic studies (Iyer et al., 2018; Singh et al., 2019; Yusuff et al., 2020). Our findings support this idea with genetic and biochemical interactions between human and *Drosophila* orthologs of SLC25A1 and MRPL40. These data led us to speculate that impaired mitochondrial protein synthesis and proteostasis likely contribute to the neurodevelopmental phenotypes observed in 22q11.2 microdeletion syndrome. We argue that this defective mitochondrial protein synthesis and proteostasis could be a mechanism shared across multiple microdeletions and neurodevelopmental disorders. For example, there are two microdeletion syndromes that encode genes required for mitochondrial protein synthesis and proteostasis. The 17q12 microdeleted locus encodes the mitochondrial rRNA methyltransferase 1 gene (MRM1, OMIM 618099 and 614527) and the 16p11.2 microdeleted locus, which encodes the mitochondrial Tu translation elongation factor gene (TUFM, OMIM 602389 and 613444). Furthermore, sufficiently powered genome-wide association studies further bolster the case for mitochondrial proteostasis in neurodevelopmental and psychiatric disorders. Noncoding regions in the mitochondrial ribosome subunit MRPS33 and the aminoacyl-tRNA synthetase DARS2 genes significantly associate with schizophrenia, autism spectrum disorder, and mood disorders risk (Schizophrenia Working Group of the Psychiatric Genomics Consortium, 2018; Cross-Disorder Group of the Psychiatric Genomics Consortium, 2019). Our studies also support a role of mitochondrial proteostasis in neurodevelopmental and psychiatric disorders since the expression of mitochondrial ribosome subunit mRNAs is neurodevelopmentally regulated and altered in schizophrenia, in a neuronal type-selective manner (Fig. 5; Extended Data Fig. 5-1). Recent studies in human schizophrenia brains show that mRNAs encoding mitochondrial proteins are reduced in affected individuals (Glausier et al., 2020). This suggests that the reduced mitochondrial ribosome mRNA expression in schizophrenia neurons reported here may reflect generalized defects in mitochondria in schizophrenia-affected individuals.

Our findings also raise questions about critical periods of brain vulnerability for exposure to antibiotics targeting mitochondrial ribosomes (Fig. 5*A*; Extended Data Fig. 5-1). We speculate that, if the fetal and adolescent brain has an increased demand for mitochondrial ribosome activity, as suggested by their expression patterns, then exposure to antibiotics during these critical periods could impair their neurodevelopment in genetically susceptible individuals (Rice and Barone, 2000). We bring forward this speculation founded on the following epidemiological observations. Tetracycline derivatives are omnipresent in the environment and a pervasive presence in the food supply chain (Daghrir and Drogui, 2013; Welsh et al., 2019). Furthermore, the dose of tetracycline derivatives capable of affecting SLC25A1 mutant cells (Fig. 4; Extended Data Fig. 4-1; ~1 μg/ml or ~2.25 μM) is just threefold below the FDA-approved limit for tetracycline antibiotics in dairy foods (FDA, 2015).

We propose that the synthetic and degradative machineries that maintain mitochondrial proteostasis are developmentally regulated machineries controlling synapse development, function, and plasticity. Thus, mitochondrial proteostasis may act as a hub where genetic, environmental, and xenobiotic insults could converge to increase the risk of neurodevelopmental and psychiatric disorders.

References

Aboulhouda S, Di Santo R, Therizols G, Weinberg D (2017) Accurate, streamlined analysis of mRNA translation by sucrose gradient fractionation. Bio Protoc 7:e2573.

Akbergenov R, Duscha S, Fritz AK, Juskeviciene R, Oishi N, Schmitt K, Shcherbakov D, Teo Y, Boukari H, Freihofer P, Isnard-Petit P, Oettinghaus B, Frank S, Thiam K, Rehrauer H, Westhof E, Schacht J, Eckert A, Wolfer D, Böttger EC (2018) Mutant MRPS5 affects mitoribosomal accuracy and confers stress-related behavioral alterations. EMBO Rep 19:e46193.

Amunts A, Brown A, Bai XC, Llacer JL, Hussain T, Emsley P, Long F, Murshudov G, Scheres SH, Ramakrishnan V (2014) Structure of the yeast mitochondrial large ribosomal subunit. Science 343:1485–1489.

Antonicka H, Shoubridge EA (2015) Mitochondrial RNA granules are centers for posttranscriptional RNA processing and ribosome biogenesis. Cell Rep 10:920–932.

Arion D, Corradi JP, Tang S, Datta D, Boothe F, He A, Cacace AM, Zaczek R, Albright CF, Tseng G, Lewis DA (2015) Distinctive transcriptome alterations of prefrontal pyramidal neurons in schizophrenia and schizoaffective disorder. Mol Psychiatry 20:1397–1405.

Arion D, Huo Z, Enwright JF, Corradi JP, Tseng G, Lewis DA (2017) Transcriptome alterations in prefrontal pyramidal cells distinguish schizophrenia from bipolar and major depressive disorders. Biol Psychiatry 82:594–600.

Arroyo JD, Jourdain AA, Calvo SE, Ballarano CA, Doench JG, Root DE, Mootha VK (2016) A genome-wide CRISPR death screen identifies genes essential for oxidative phosphorylation. Cell Metab 24:875–885.

Bassell GJ, Warren ST (2008) Fragile X syndrome: loss of local mRNA regulation alters synaptic development and function. Neuron 60:201–214.

Bier E (2005) *Drosophila*, the golden bug, emerges as a tool for human genetics. Nat Rev Genet 6:9–23.

Bilousova TV, Dansie L, Ngo M, Aye J, Charles JR, Ethell DW, Ethell IM (2009) Minocycline promotes dendritic spine maturation and improves behavioural performance in the fragile X mouse model. J Med Genet 46:94–102.

Bindea G, Mlecnik B, Hackl H, Charoentong P, Tosolini M, Kirilovsky A, Fridman WH, Pages F, Trajanoski Z, Galon J (2009) ClueGO: a Cytoscape plug-in to decipher functionally grouped gene ontology and pathway annotation networks. Bioinformatics 25:1091–1093.

Schizophrenia Working Group of the Psychiatric Genomics Consortium (2018) Genomic dissection of bipolar disorder and schizophrenia, including 28 subphenotypes. Cell 173:1705–1715.e16.

Burman JL, Pickles S, Wang C, Sekine S, Vargas JN, Zhang Z, Youle AM, Nezich CL, Wu X, Hammer JA, Youle RJ (2017) Mitochondrial fission facilitates the selective mitophagy of protein aggregates. J Cell Biol 216:3231–3247.

Cardoso-Moreira M, Halbert J, Valloton D, Velten B, Chen C, Shao Y, Liechti A, Ascenção K, Rummel C, Ovchinnikova S, Mazin PV, Xenarios I, Harshman K, Mort M, Cooper DN, Sandi C, Soares MJ, Ferreira PG, Afonso S, Carneiro M, et al. (2019) Gene expression across mammalian organ development. Nature 571:505–509.

Chatzispyrou IA, Held NM, Mouchiroud L, Auwerx J, Houtkooper RH (2015) Tetracycline antibiotics impair mitochondrial function and its experimental use confounds research. Cancer Res 75:4446–4449.

Comstra HS, McArthy J, Rudin-Rush S, Hartwig C, Gokhale A, Zlatic SA, Blackburn JB, Werner E, Petris M, D'Souza P, Panuwet P, Barr DB, Lupashin V, Vrailas-Mortimer A, Faundez V (2017) The interactome of the copper transporter ATP7A belongs to a network of neurodevelopmental and neurodegeneration factors. Elife 6:e24722.

Cross-Disorder Group of the Psychiatric Genomics Consortium (2019) Genomic relationships, novel loci, and pleiotropic mechanisms across eight psychiatric disorders. Cell 179:1469–1482.e11.

Couvillion MT, Soto IC, Shipkovenska G, Churchman LS (2016) Synchronized mitochondrial and cytosolic translation programs. Nature 533:499–503.

Daghrir R, Drogui P (2013) Tetracycline antibiotics in the environment: a review. Environ Chem Lett 11:209–227.

Devaraju P, Yu J, Eddins D, Mellado-Lagarde MM, Earls LR, Westmoreland JJ, Quarato G, Green DR, Zakharenko SS (2017) Haploinsufficiency of the 22q11.2 microdeletion gene Mrpl40 disrupts short-term synaptic plasticity and working memory through dysregulation of mitochondrial calcium. Mol Psychiatry 22:1313–1326.

Divakaruni AS, Paradyse A, Ferrick DA, Murphy AN, Jastroch M (2014) Analysis and interpretation of microplate-based oxygen consumption and pH data. Methods Enzymol 547:309–354.

Drawz SM, Bonomo RA (2010) Three decades of beta-lactamase inhibitors. Clin Microbiol Rev 23:160–201.

Dziembowska M, Pretto DI, Janusz A, Kaczmarek L, Leigh MJ, Gabriel N, Durbin-Johnson B, Hagerman RJ, Tassone F (2013) High MMP-9 activity levels in fragile X syndrome are lowered by minocycline. Am J Med Genet A 161A:1897–1903.

Enwright JF III, Huo Z, Arion D, Corradi JP, Tseng G, Lewis DA (2018) Transcriptome alterations of prefrontal cortical parvalbumin neurons in schizophrenia. Mol Psychiatry 23:1606–1613.

Faundez V, Krauss R, Holuigue L, Garrido J, Gonzalez A (1992) Epidermal growth factor receptor in synaptic fractions of the rat central nervous system. J Biol Chem 267:20363–20370.

FDA (2015) Milk drug residue sampling survey. Available at https://www.fda.gov/media/91217/download.

Feoktistova M, Geserick P, Leverkus M (2016) Crystal violet assay for determining viability of cultured cells. Cold Spring Harb Protoc 2016:pdb.prot087379.

Fernandez A, Meechan DW, Karpinski BA, Paronett EM, Bryan CA, Rutz HL, Radin EA, Lubin N, Bonner ER, Popratiloff A, Rothblat LA, Maynard TM, LaMantia AS (2019) Mitochondrial dysfunction leads to cortical under-connectivity and cognitive impairment. Neuron 102:1127–1142.e3.

Fujiki Y, Hubbard AL, Fowler S, Lazarow PB (1982) Isolation of intracellular membranes by means of sodium carbonate treatment: application to endoplasmic reticulum. J Cell Biol 93:97–102.

Gardeitchik T, Mohamed M, Ruzzenente B, Karall D, Guerrero-Castillo S, Dalloyaux D, van den Brand M, van Kraaij S, van Asbeck E, Assouline Z, Rio M, de Lonlay P, Scholl-Buergi S, Wolthuis DF, Hoischen A, Rodenburg RJ, Sperl W, Urban Z, Brandt U, Mayr JA, et al. (2018) Bi-allelic mutations in the mitochondrial ribosomal protein MRPS2 cause sensorineural hearing loss, hypoglycemia, and multiple OXPHOS complex deficiencies. Am J Hum Genet 102:685–695.

Garrido-Mesa N, Zarzuelo A, Gálvez J (2013) Minocycline: far beyond an antibiotic. Br J Pharmacol 169:337–352.

Gatto CL, Broadie K (2011) *Drosophila* modeling of heritable neurodevelopmental disorders. Curr Opin Neurobiol 21:834–841.

Giovanoli S, Engler H, Engler A, Richetto J, Feldon J, Riva MA, Schedlowski M, Meyer U (2016) Preventive effects of minocycline in a neurodevelopmental two-hit model with relevance to schizophrenia. Transl Psychiatry 6:e772.

Giurgiu M, Reinhard J, Brauner B, Dunger-Kaltenbach I, Fobo G, Frishman G, Montrone C, Ruepp A (2019) CORUM: the comprehensive resource of mammalian protein complexes-2019. Nucleic Acids Res 47:D559–D563.

Glausier JR, Enwright JF, Lewis DA (2020) Diagnosis- and cell type-specific mitochondrial functional pathway signatures in schizophrenia and bipolar disorder. Am J Psychiatry 177:1140–1150.

Gokhale A, Larimore J, Werner E, So L, Moreno-De-Luca A, Lese-Martin C, Lupashin VV, Smith Y, Faundez V (2012) Quantitative proteomic and genetic analyses of the schizophrenia susceptibility factor dysbindin identify novel roles of the biogenesis of lysosome-related organelles complex 1. J Neurosci 32:3697–3711.

Gokhale A, Hartwig C, Freeman AA, Bassell JL, Zlatic SA, Sapp Savas C, Vadlamudi T, Abudulai F, Pham TT, Crocker A, Werner E, Wen Z, Repetto GM, Gogos JA, Claypool SM, Forsyth JK, Bearden CE, Glausier J, Lewis DA, Seyfried NT, et al. (2019) Systems analysis of the 22q11.2 microdeletion syndrome converges on a mitochondrial interactome necessary for synapse function and behavior. J Neurosci 39:3561–3581.

Guna A, Butcher NJ, Bassett AS (2015) Comparative mapping of the 22q11.2 deletion region and the potential of simple model organisms. J Neurodev Disord 7:18.

Han K, Holder JL Jr, Schaaf CP, Lu H, Chen H, Kang H, Tang J, Wu Z, Hao S, Cheung SW, Yu P, Sun H, Breman AM, Patel A, Lu HC, Zoghbi HY (2013) SHANK3 overexpression causes manic-like behaviour with unique pharmacogenetic properties. Nature 503:72–77.

Hawrylycz MJ, Lein ES, Guillozet-Bongaarts AL, Shen EH, Ng L, Miller JA, van de Lagemaat LN, Smith KA, Ebbert A, Riley ZL, Abajian C, Beckmann CF, Bernard A, Bertagnolli D, Boe AF, Cartagena PM, Chakravarty MM, Chapin M, Chong J, Dalley RA, et al. (2012) An anatomically comprehensive atlas of the adult human brain transcriptome. Nature 489:391–399.

Hendricks JC, Finn SM, Panckeri KA, Chavkin J, Williams JA, Sehgal A, Pack AI (2000) Rest in *Drosophila* is a sleep-like state. Neuron 25:129–138.

Higginbotham L, Ping L, Dammer EB, Duong DM, Zhou M, Gearing M, Johnson EC, Hajjar I, Lah JJ, Levey AI, Seyfried NT (2019) Integrated proteomics reveals brain-based cerebrospinal fluid biomarkers in asymptomatic and symptomatic Alzheimer's disease. bioRxiv

Hoftman GD, Volk DW, Bazmi HH, Li S, Sampson AR, Lewis DA (2015) Altered cortical expression of GABA-related genes in schizophrenia: illness progression vs developmental disturbance. Schizophr Bull 41:180–191.

Houtkooper RH, Mouchiroud L, Ryu D, Moullan N, Katsyuba E, Knott G, Williams RW, Auwerx J (2013) Mitonuclear protein imbalance as a conserved longevity mechanism. Nature 497:451–457.

Iyer J, Singh MD, Jensen M, Patel P, Pizzo L, Huber E, Koerselman H, Weiner AT, Lepanto P, Vadodaria K, Kubina A, Wang Q, Talbert A, Yennawar S, Badano J, Manak JR, Rolls MM, Krishnan A, Girirajan S (2018) Pervasive genetic interactions modulate neurodevelopmental defects of the autism-associated 16p11.2 deletion in *Drosophila melanogaster*. Nat Commun 9:2548.

Jensen M, Girirajan S (2019) An interaction-based model for neuropsychiatric features of copy-number variants. PLoS Genet 15:e1007879.

Jia L, Kaur J, Stuart RA (2009) Mapping of the Saccharomyces cerevisiae Oxa1-mitochondrial ribosome interface and identification of MrpL40, a ribosomal protein in close proximity to Oxa1 and critical for oxidative phosphorylation complex assembly. Eukaryot Cell 8:1792–1802.

Jonas RK, Montojo CA, Bearden CE (2014) The 22q11.2 deletion syndrome as a window into complex neuropsychiatric disorders over the lifespan. Biol Psychiatry 75:351–360.

Kalghatgi S, Spina CS, Costello JC, Liesa M, Morones-Ramirez JR, Slomovic S, Molina A, Shirihai OS, Collins JJ (2013) Bactericidal antibiotics induce mitochondrial dysfunction and oxidative damage in Mammalian cells. Sci Transl Med 5:192ra185.

Kirov G (2015) CNVs in neuropsychiatric disorders. Hum Mol Genet 24:R45–R49.

Koripella RK, Sharma MR, Risteff P, Keshavan P, Agrawal RK (2019) Structural insights into unique features of the human mitochondrial ribosome recycling. Proc Natl Acad Sci USA 116:8283–8288.

Kuleshov MV, Jones MR, Rouillard AD, Fernandez NF, Duan Q, Wang Z, Koplev S, Jenkins SL, Jagodnik KM, Lachmann A, McDermott MG, Monteiro CD, Gundersen GW, Ma'ayan A (2016) Enrichr: a comprehensive gene set enrichment analysis web server 2016 update. Nucleic Acids Res 44:W90–W97.

Kume T, Kawato Y, Osakada F, Izumi Y, Katsuki H, Nakagawa T, Kaneko S, Niidome T, Takada-Takatori Y, Akaike A (2008) Dibutyryl cyclic AMP induces differentiation of human neuroblastoma SH-SY5Y cells into a noradrenergic phenotype. Neurosci Lett 443:199–203.

Lake NJ, Webb BD, Stroud DA, Richman TR, Ruzzenente B, Compton AG, Mountford HS, Pulman J, Zangarelli C, Rio M, Boddaert N, Assouline Z, Sherpa MD, Schadt EE, Houten SM, Byrnes J, McCormick EM, Zolkipli-Cunningham Z, Haude K, Zhang Z, et al. (2017) Biallelic mutations in MRPS34 lead to instability of the small mitoribosomal subunit and Leigh syndrome. Am J Hum Genet 101:239–254.

Landgraf M, Sanchez-Soriano N, Technau GM, Urban J, Prokop A (2003) Charting the *Drosophila* neuropile: a strategy for the standardised characterisation of genetically amenable neurites. Dev Biol 260:207–225.

Lee CE, Singleton KS, Wallin M, Faundez V (2020) Rare genetic diseases: nature's experiments on human development. iScience 23:101123.

Lewis DA, Levitt P (2002) Schizophrenia as a disorder of neurodevelopment. Annu Rev Neurosci 25:409–432.

Lewis DA, Curley AA, Glausier JR, Volk DW (2012) Cortical parvalbumin interneurons and cognitive dysfunction in schizophrenia. Trends Neurosci 35:57–67.

Li H, Hurlburt AJ, Tennessen JM (2018) A *Drosophila* model of combined D-2- and L-2-hydroxyglutaric aciduria reveals a mechanism linking mitochondrial citrate export with oncometabolite accumulation. Dis Model Mech 11:dmm035337.

Lightowlers RN, Taylor RW, Turnbull DM (2015) Mutations causing mitochondrial disease: what is new and what challenges remain? Science 349:1494–1499.

Liu YJ, McIntyre RL, Janssens GE, Williams EG, Lan J, van Weeghel M, Schomakers B, van der Veen H, van der Wel NN, Yao P, Mair WB, Aebersold R, MacInnes AW, Houtkooper RH (2020) Mitochondrial translation and dynamics synergistically extend lifespan in C. elegans through HLH-30. J Cell Biol 219: e201907067.

Lottes EN, Cox DN (2020) Homeostatic roles of the proteostasis network in dendrites. Front Cell Neurosci 14:264.

Mahr A, Aberle H (2006) The expression pattern of the *Drosophila* vesicular glutamate transporter: a marker protein for motoneurons and glutamatergic centers in the brain. Gene Expr Patterns 6:299–309.

Majd H, King MS, Smith AC, Kunji ER (2018) Pathogenic mutations of the human mitochondrial citrate carrier SLC25A1 lead to impaired citrate export required for lipid, dolichol, ubiquinone and sterol synthesis. Biochim Biophys Acta Bioenerg 1859:1–7.

Malhotra D, Sebat J (2012) CNVs: harbingers of a rare variant revolution in psychiatric genetics. Cell 148:1223–1241.

Marullo R, Werner E, Degtyareva N, Moore B, Altavilla G, Ramalingam SS, Doetsch PW (2013) Cisplatin induces a mitochondrial-ROS response that contributes to cytotoxicity depending on mitochondrial redox status and bioenergetic functions. PLoS One 8:e81162.

Matthews DE, Hessler RA, Denslow ND, Edwards JS, O'Brien TW (1982) Protein composition of the bovine mitochondrial ribosome. J Biol Chem 257:8788–8794.

Maynard TM, Meechan DW, Dudevoir ML, Gopalakrishna D, Peters AZ, Heindel CC, Sugimoto TJ, Wu Y, Lieberman JA, Lamantia AS (2008) Mitochondrial localization and function of a subset of 22q11 deletion syndrome candidate genes. Mol Cell Neurosci 39:439–451.

McDonald-McGinn DM, Sullivan KE, Marino B, Philip N, Swillen A, Vorstman JA, Zackai EH, Emanuel BS, Vermeesch JR, Morrow BE, Scambler PJ, Bassett AS (2015) 22q11.2 deletion syndrome. Nat Rev Dis Primers 1:15071.

Menon KP, Carrillo RA, Zinn K (2013) Development and plasticity of the *Drosophila* larval neuromuscular junction. Wiley Interdiscip Rev Dev Biol 2:647–670.

Miller JA, Ding SL, Sunkin SM, Smith KA, Ng L, Szafer A, Ebbert A, Riley ZL, Royall JJ, Aiona K, Arnold JM, Bennet C, Bertagnolli D, Brouner K, Butler S, Caldejon S, Carey A, Cuhaciyan C, Dalley RA, Dee N, et al. (2014) Transcriptional landscape of the prenatal human brain. Nature 508:199–206.

Moullan N, Mouchiroud L, Wang X, Ryu D, Williams EG, Mottis A, Jovaisaite V, Frochaux MV, Quiros PM, Deplancke B, Houtkooper RH, Auwerx J (2015) Tetracyclines disturb mitochondrial function across eukaryotic models: a call for caution in biomedical research. Cell Rep 10:1681–1691.

Mullin AP, Gokhale A, Larimore J, Faundez V (2011) Cell biology of the BLOC-1 complex subunit dysbindin, a schizophrenia susceptibility gene. Mol Neurobiol 44:53–64.

Munch C, Harper JW (2016) Mitochondrial unfolded protein response controls matrix pre-RNA processing and translation. Nature 534:710–713.

Nagy A, Delgado-Escueta AV (1984) Rapid preparation of synaptosomes from mammalian brain using nontoxic isoosmotic gradient material (Percoll). J Neurochem 43:1114–1123.

Nelson SB, Valakh V (2015) Excitatory/inhibitory balance and circuit homeostasis in autism spectrum disorders. Neuron 87:684–698.

Nimmo GA, Venkatesh S, Pandey AK, Marshall CR, Hazrati LN, Blaser S, Ahmed S, Cameron J, Singh K, Ray PN, Suzuki CK, Yoon G (2019) Biallelic mutations of LONP1 encoding the mitochondrial LonP1 protease cause pyruvate dehydrogenase deficiency and profound neurodegeneration with progressive cerebellar atrophy. Hum Mol Genet 28:290–306.

Nota B, Struys EA, Pop A, Jansen EE, Fernandez Ojeda MR, Kanhai WA, Kranendijk M, van Dooren SJ, Bevova MR, Sistermans EA, Nieuwint AW, Barth M, Ben-Omran T, Hoffmann GF, de Lonlay P, McDonald MT, Meberg A, Muntau AC, Nuoffer JM, Parini R, et al. (2013) Deficiency in SLC25A1, encoding the mitochondrial citrate carrier, causes combined D-2- and L-2-hydroxyglutaric aciduria. Am J Hum Genet 92:627–631.

Ogunbona OB, Claypool SM (2019) Emerging roles in the biogenesis of cytochrome c oxidase for members of the mitochondrial carrier family. Front Cell Dev Biol 7:3.

Palmieri F (2014) Mitochondrial transporters of the SLC25 family and associated diseases: a review. J Inherit Metab Dis 37:565–575.

Pei L, Wallace DC (2018) Mitochondrial etiology of neuropsychiatric disorders. Biol Psychiatry 83:722–730.

Perez-Cornejo P, Gokhale A, Duran C, Cui Y, Xiao Q, Hartzell HC, Faundez V (2012) Anoctamin 1 (Tmem16A) Ca^{2+}-activated chloride channel stoichiometrically interacts with an ezrin-radixin-moesin network. Proc Natl Acad Sci USA 109:10376–10381.

Perez-Riverol Y, Xu QW, Wang R, Uszkoreit J, Griss J, Sanchez A, Reisinger F, Csordas A, Ternent T, Del-Toro N, Dianes JA, Eisenacher M, Hermjakob H, Vizcaíno JA (2016) PRIDE Inspector Toolsuite: moving toward a universal visualization tool for proteomics data standard formats and quality assessment of ProteomeXchange datasets. Mol Cell Proteomics 15:305–317.

Pickles S, Vigie P, Youle RJ (2018) Mitophagy and quality control mechanisms in mitochondrial maintenance. Curr Biol 28:R170–R185.

Pietrocola F, Galluzzi L, Bravo-San Pedro JM, Madeo F, Kroemer G (2015) Acetyl coenzyme A: a central metabolite and second messenger. Cell Metab 21:805–821.

Ping L, Duong DM, Yin L, Gearing M, Lah JJ, Levey AI, Seyfried NT (2018) Global quantitative analysis of the human brain proteome in Alzheimer's and Parkinson's disease. Sci Data 5:180036.

Rice D, Barone S Jr (2000) Critical periods of vulnerability for the developing nervous system: evidence from humans and animal models. Environ Health Perspect 108 Suppl 3:511–533.

Richter U, Lahtinen T, Marttinen P, Myohanen M, Greco D, Cannino G, Jacobs HT, Lietzen N, Nyman TA, Battersby BJ (2013) A mitochondrial ribosomal and RNA decay pathway blocks cell proliferation. Curr Biol 23:535–541.

Richter U, Lahtinen T, Marttinen P, Suomi F, Battersby BJ (2015) Quality control of mitochondrial protein synthesis is required for membrane integrity and cell fitness. J Cell Biol 211:373–389.

Robinson-Shelton A, Malow BA (2016) Sleep disturbances in neurodevelopmental disorders. Curr Psychiatry Rep 18:6.

Rooney JP, Ryde IT, Sanders LH, Howlett EH, Colton MD, Germ KE, Mayer GD, Greenamyre JT, Meyer JN (2015) PCR based determination of mitochondrial DNA copy number in multiple species. Methods Mol Biol 1241:23–38.

Rubenstein JL, Merzenich MM (2003) Model of autism: increased ratio of excitation/inhibition in key neural systems. Genes Brain Behav 2:255–267.

Ruprecht JJ, Kunji ER (2019) The SLC25 mitochondrial carrier family: structure and mechanism. Trends Biochem Sci 45:244–258.

Rutkowski TP, Schroeder JP, Gafford GM, Warren ST, Weinshenker D, Caspary T, Mulle JG (2017) Unraveling the genetic architecture of copy number variants associated with schizophrenia and other neuropsychiatric disorders. J Neurosci Res 95:1144–1160.

Ryder PV, Vistein R, Gokhale A, Seaman MN, Puthenveedu MA, Faundez V (2013) The WASH complex, an endosomal Arp2/3 activator, interacts with the Hermansky-Pudlak syndrome complex BLOC-1 and its cargo phosphatidylinositol-4-kinase type IIalpha. Mol Biol Cell 24:2269–2284.

Shannon P, Markiel A, Ozier O, Baliga NS, Wang JT, Ramage D, Amin N, Schwikowski B, Ideker T (2003) Cytoscape: a software environment for

integrated models of biomolecular interaction networks. Genome Res 13:2498–2504.
Shaw PJ, Cirelli C, Greenspan RJ, Tononi G (2000) Correlates of sleep and waking in *Drosophila melanogaster*. Science 287:1834–1837.
Shpilka T, Haynes CM (2018) The mitochondrial UPR: mechanisms, physiological functions and implications in ageing. Nat Rev Mol Cell Biol 19:109–120.
Shutt TE, Shadel GS (2010) A compendium of human mitochondrial gene expression machinery with links to disease. Environ Mol Mutagen 51:360–379.
Singh MD, Jensen M, Lasser M, Huber E, Yusuff T, Pizzo L, Lifschutz B, Desai I, Kubina A, Yennawar S, Kim S, Iyer J, Rincon-Limas DE, Lowery LA, Girirajan S (2019) NCBP2 modulates neurodevelopmental defects of the 3q29 deletion in *Drosophila* and *X. laevis* models. bioRxiv 614750.
Skrtic M, Sriskanthadevan S, Jhas B, Gebbia M, Wang X, Wang Z, Hurren R, Jitkova Y, Gronda M, Maclean N, Lai CK, Eberhard Y, Bartoszko J, Spagnuolo P, Rutledge AC, Datti A, Ketela T, Moffat J, Robinson BH, Cameron JH, et al. (2011) Inhibition of mitochondrial translation as a therapeutic strategy for human acute myeloid leukemia. Cancer Cell 20:674–688.
Srivatsan SR, McFaline-Figueroa JL, Ramani V, Saunders L, Cao J, Packer J, Pliner HA, Jackson DL, Daza RM, Christiansen L, Zhang F, Steemers F, Shendure J, Trapnell C (2020) Massively multiplex chemical transcriptomics at single cell resolution. Science 367:45–51.
Sudhof TC (2008) Neuroligins and neurexins link synaptic function to cognitive disease. Nature 455:903–911.
Suhl JA, Chopra P, Anderson BR, Bassell GJ, Warren ST (2014) Analysis of FMRP mRNA target datasets reveals highly associated mRNAs mediated by G-quadruplex structures formed via clustered WGGA sequences. Hum Mol Genet 23:5479–5491.
Sun N, Youle RJ, Finkel T (2016) The mitochondrial basis of aging. Mol Cell 61:654–666.
Sutton MA, Schuman EM (2006) Dendritic protein synthesis, synaptic plasticity, and memory. Cell 127:49–58.
Taanman JW (1999) The mitochondrial genome: structure, transcription, translation and replication. Biochim Biophys Acta 1410:103–123.
Tasic B, Yao Z, Graybuck LT, Smith KA, Nguyen TN, Bertagnolli D, Goldy J, Garren E, Economo MN, Viswanathan S, Penn O, Bakken T, Menon V, Miller J, Fong O, Hirokawa KE, Lathia K, Rimorin C, Tieu M, Larsen R, et al. (2018) Shared and distinct transcriptomic cell types across neocortical areas. Nature 563:72–78.
Wallace DC (2010) Mitochondrial DNA mutations in disease and aging. Environ Mol Mutagen 51:440–450.
Wallace DC, Fan W, Procaccio V (2010) Mitochondrial energetics and therapeutics. Annu Rev Pathol 5:297–348.
Warde-Farley D, Donaldson SL, Comes O, Zuberi K, Badrawi R, Chao P, Franz M, Grouios C, Kazi F, Lopes CT, Maitland A, Mostafavi S, Montojo J, Shao Q, Wright G, Bader GD, Morris Q (2010) The GeneMANIA prediction server: biological network integration for gene prioritization and predicting gene function. Nucleic Acids Res 38:W214–W220.
Wellen KE, Hatzivassiliou G, Sachdeva UM, Bui TV, Cross JR, Thompson CB (2009) ATP-citrate lyase links cellular metabolism to histone acetylation. Science 324:1076–1080.
Welsh JA, Braun H, Brown N, Um C, Ehret K, Figueroa J, Boyd Barr D (2019) Production-related contaminants (pesticides, antibiotics and hormones) in organic and conventionally produced milk samples sold in the USA. Public Health Nutr 22:2972–2980.
Werner T, Becher I, Sweetman G, Doce C, Savitski MM, Bantscheff M (2012) High-resolution enabled TMT 8-plexing. Anal Chem 84:7188–7194.
Wilson DN (2014) Ribosome-targeting antibiotics and mechanisms of bacterial resistance. Nat Rev Microbiol 12:35–48.
Wu L, Candille SI, Choi Y, Xie D, Jiang L, Li-Pook-Than J, Tang H, Snyder M (2013) Variation and genetic control of protein abundance in humans. Nature 499:79–82.
Yizhar O, Fenno LE, Prigge M, Schneider F, Davidson TJ, O'Shea DJ, Sohal VS, Goshen I, Finkelstein J, Paz JT, Stehfest K, Fudim R, Ramakrishnan C, Huguenard JR, Hegemann P, Deisseroth K (2011) Neocortical excitation/inhibition balance in information processing and social dysfunction. Nature 477:171–178.
Yusuff T, Jensen M, Yennawar S, Pizzo L, Karthikeyan S, Gould DJ, Sarker A, Matsui Y, Iyer J, Lai ZC, Girirajan S (2020) *Drosophila* models of pathogenic copy-number variant genes show global and non-neuronal defects during development. PLoS Genet 16:e1008792.
Zeng R, Smith E, Barrientos A (2018) Yeast mitoribosome large subunit assembly proceeds by hierarchical incorporation of protein clusters and modules on the inner membrane. Cell Metab 27:645–656.e7.
Zhang YQ, Bailey AM, Matthies HJ, Renden RB, Smith MA, Speese SD, Rubin GM, Broadie K (2001) *Drosophila* fragile X-related gene regulates the MAP1B homolog Futsch to control synaptic structure and function. Cell 107:591–603.
Zoghbi HY, Bear MF (2012) Synaptic dysfunction in neurodevelopmental disorders associated with autism and intellectual disabilities. Cold Spring Harb Perspect Biol 4:a009886.